

12

AD

AD-E400 816

TECHNICAL REPORT ARLCD-TR-82002

**CHARCOAL REGENERATION - PART III.  
MECHANISM OF RDX ADSORPTION**

**JEROME HABERMAN  
THOMAS C. CASTORINA**

**APRIL 1982**



**US ARMY ARMAMENT RESEARCH AND DEVELOPMENT COMMAND  
LARGE CALIBER  
WEAPON SYSTEMS LABORATORY  
DOVER, NEW JERSEY**

**APPROVED FOR PUBLIC RELEASE; DISTRIBUTION UNLIMITED.**

**DTIC  
ELECTE  
JUL 30 1982**

**B**

20

AD A117592

DTIC FILE COPY

The views, opinions, and/or findings contained in this report are those of the author(s) and should not be construed as an official Department of the Army position, policy or decision, unless so designated by other documentation.

The citation in this report of the names of commercial firms or commercially available products or services does not constitute official endorsement by or approval of the U.S. Government.

Destroy this report when no longer needed. Do not return to the originator.

UNCLASSIFIED

SECURITY CLASSIFICATION OF THIS PAGE (When Data Entered)

REPORT DOCUMENTATION PAGE		READ INSTRUCTIONS BEFORE COMPLETING FORM
1. REPORT NUMBER	2. GOVT ACCESSION NO.	3. RECIPIENT'S CATALOG NUMBER
Technical Report ARJCD-TE-82002		
4. TITLE (and Subtitle)		5. TYPE OF REPORT & PERIOD COVERED
CHARCOAL REGENERATION - PART III. MECHANISM OF RDX ADSORPTION		
		6. PERFORMING ORG. REPORT NUMBER
7. AUTHOR(s)		8. CONTRACT OR GRANT NUMBER(s)
Jerome Haberman Thomas C. Castorina		3627-01-001
9. PERFORMING ORGANIZATION NAME AND ADDRESS		10. PROGRAM ELEMENT PROJECT TASK AREA & WORK UNIT NUMBERS
ARRADCOM, LCWSL Energetic Materials Division (DRDAR-LCE) Dover, NJ 07801		
11. CONTROLLING OFFICE NAME AND ADDRESS		12. REPORT DATE
ARRADCOM, TSD STINFO Div (DRDAR-TSS) Dover, NJ 07801		April 1982
		13. NUMBER OF PAGES
		59
14. MONITORING AGENCY NAME & ADDRESS (if different from Controlling Office)		15. SECURITY CLASS (of this report)
U.S. Army Toxic and Hazardous Materials Agency ATTN: DRXTH-TE-D Aberdeen Proving Ground, MD 21010		Unclassified
		15a. DECLASSIFICATION/DOWNGRADING SCHEDULE
16. DISTRIBUTION STATEMENT (of this Report)		
Approved for public release; distribution unlimited.		
17. DISTRIBUTION STATEMENT (of the abstract entered in Block 20, if different from Report)		
18. SUPPLEMENTARY NOTES		
This study was funded under the Environmental Quality R&D program administered by the U.S. Army Toxic and Hazardous Materials Agency.  (continued)		
19. KEY WORDS (Continue on reverse side if necessary and identify by block number)		
Activated carbon	Water adsorption/desorption	Solvent regeneration
Pretreatment	Pore size distribution	
Batch cycling	Isotherms	
Column cycling	Degradation of carbon	
Cycling properties	RDX adsorption	
20. ABSTRACT (Continue on reverse side if necessary and identify by block number)		
Cyclotrimethylenetrinitramine (RDX) adsorption and solvent desorption cycling of activated carbon (FS300) have been studied as a function of various pretreatments. As with a previous TNT study, preferential plugging of pores by pretreatments did not enhance the regeneration of the FS300. Using water adsorption/desorption isotherms, the characteristics of a carbon with improved cycling properties has been elucidated. These properties are in agreement with those characteristics previously found in the study with TNT and are  (continued)		

UNCLASSIFIED

SECURITY CLASSIFICATION OF THIS PAGE(When Data Entered)

18. SUPPLEMENTARY NOTES (continued): Technical Reports ARLCD-TR-77065 and ARLCD-TR-80012 are also related to this program.

20. ABSTRACT (continued):

based to a shift to a larger pore volume, increased numbers of pore body diameters in the mesopore range, and an increase in the ratio of pore opening to pore body diameter. The mechanism of RDX adsorption on FS300 has been elucidated and compared to that of TNT.

UNCLASSIFIED

SECURITY CLASSIFICATION OF THIS PAGE(When Data Entered)

# ACKNOWLEDGMENT

The authors thank Professor F. J. Micale of Lehigh University, Bethlehem, PA, for the significant contributions he has made under contract DAA-29-76-D00100 on the water adsorption measurements, and for many helpful discussions dealing with the interpretation of these measurements as related to the cycling of activated carbon.

This project was funded by the U.S. Army Toxic and Hazardous Materials Agency, Edgewood Arsenal, Aberdeen Proving Ground, MD.

APPROVED FOR	✓
DATE	
BY	
REVIEWED	
DATE	
BY	
APPROVED FOR	
DATE	
BY	
DIST	
A	



## CONTENTS

	Page
Introduction	
Experimental	
Charcoal Preparation	1
Materials	2
Pretreatments	2
Water Adsorption Isotherms	2
Ultraviolet Analysis of Aqueous Solutions	2
Column Cycling (Adsorption-Desorption)	3
Batch Cycling (Adsorption-Desorption)	4
Results and Discussion	5
Surface Area Degradation	5
Adsorption/Desorption Isotherms	7
Conclusions	9
References	11
Distribution List	31

## TABLES

	Page
1 Rates of degradation of pretreated carbons and integrated areas under the degradation curve	13
2 Surface areas of pretreated carbons	14
3 Relative amount of RDX absorbed on carbons	14

## FIGURES

	Page
1 Adsorption isotherms of TNT and RDX on FS300	15
2 Linear plots of specific adsorption deactivation as a function of RDX adsorption/solvent desorption cycling according to a second order kinetic model	16
3 Electron spectrum of RDX	17
4 Electron spectrum of RDX/carbon surface complex	18
5 Low pressure water isotherms on some carbons	19
6 Change in pore opening size distribution relative to uncycled FS300 as a function of cycling	20
7 Change in pore body size distribution relative to uncycled FS300 as a function of cycling	21
8 Change in pore opening size distribution relative to FS300 of RDX cycled FS400	22
9 Change in pore body size distribution relative to FS300 of RDX cycled FS400	23
10 Change in pore opening size distribution relative to FS300 of RDX cycled hydrogen treated FS300	24
11 Change in pore body size distribution relative to FS300 of RDX cycled hydrogen treated FS300	25
12 Change in pore opening size distribution relative to FS300 of RDX cycled WITCO carbon	26
13 Change in pore body size distribution relative to FS300 of RDX cycled WITCO carbon	27
14 Change in pore opening size distribution relative to FS300 of NO and CH <sub>4</sub> treated FS300	28
15 Change in pore body size distribution relative to FS300 of NO and CH <sub>4</sub> treated FS300	29



## INTRODUCTION

Granular activated carbon (GAC) is used at Load, Assemble, and Pack Plants for the treatment of pink wastewaters. Current practice of disposal of the spent GAC is by open-field incineration, which is both costly and leads to air pollution. A more desirable method of dealing with this problem would be regeneration of the spent GAC by solvent extraction. Solvent regeneration would be cost-effective not only in extending the useful life of the absorbent, but also in its potential for recovering explosives. For the development of an efficient solvent regeneration process, an understanding of the mechanism of adsorption and of the surface properties of GAC was necessary. Previous reports, (refs 1 and 2) dwelt on the interaction of TNT with the surface of GAC. In reference 1 it was shown that the rate and extent of adsorption of TNT are strongly dependent on the particle size of the GAC (diffusion rate controlled) and are independent of pH and temperature.

The deactivation of the carbon surface was shown to involve a progressive, irreversible occlusion of the microporous structure with each successive TNT adsorption-acetone desorption cycle. The irreversibility of TNT adsorption was attributed to chemical interaction due to the active nature of the carbon and/or the pore size distribution. It was postulated that the TNT adsorbate molecules are attracted first to regions of the surface which have the highest energy. These regions are associated with various functional groups and surface carbon atoms having incomplete coordination numbers. Accordingly, the approach was to pacify the surface by reacting the high energy sites with molecules, which would then permit subsequently adsorbed TNT molecules to be easily desorbed. Characteristics of a GAC with an improved cycling capability were determined (ref 2), and it was found that this improvement is due primarily to a reduction in number of active sites, a shift to a larger pore volume, a larger ratio of pore opening to pore diameter, and an increased number of pores in the diameter range of 50 to 100Å.

As the next phase in this study of solvent regeneration of spent carbon, the investigation described in this report deals with the affect of the RDX (cyclotrimethylenetrinitramine) molecule upon the regenerative properties of some of the same GAC's used in the TNT studies. Also, the interaction of RDX with the carbon surface has been examined under the same parametric conditions employed for TNT.

## EXPERIMENTAL

### Charcoal Preparation

The activated carbon used in this study was FS300 obtained from Calgon Corporation, Pittsburgh, PA. The carbon was ground to a 40/80 mesh, washed thoroughly with distilled water, and dried at 150°C for 2 hours. Other GAC's used were FS400 from Calgon Corporation, and WITCO 337 (now designated as grade 965 from WITCO Corporation, New York, NY). These GAC's were also ground to a 40/80 mesh, water washed, and dried.

## Materials

The gases, hydrogen, methane/argon, nitric oxide, and nitrogen dioxide used in the pretreatment of charcoal were of reagent quality.

## Pretreatments

All pretreated samples were obtained from a master batch of FS300 prepared as described above. The FS300 carbon was placed in a quartz tube (50 cm by 1.6 cm) and hydrogen and 10% methane in 90% argon were allowed separately to flow through the tube at a flow rate of 2 to 3 milliliters (mL)/min. After the air was displaced, the tube was heated in a previously calibrated tube furnace to the experimental temperature and allowed to remain at this temperature for the required time. Cooling was accomplished by allowing the gas to flow until room temperature was reached.

The NO and NO<sub>2</sub> treated carbons were prepared by allowing the vapors to displace the air in stoppered flasks, and to remain in contact with the carbons at ambient temperature for the requisite time. The excess vapors were absorbed in caustic solution when preparing the samples.

The NO<sub>2</sub> treated sample was stored in a vacuum desiccator and pumped to remove excess NO<sub>2</sub>. The NO treated sample was washed with distilled water and then dried in a vacuum desiccator.

## Water Adsorption Isotherms

Water adsorption isotherms were determined gravimetrically on a quartz spring balance (Worden Quartz Products, Inc.), which had an absolute sensitivity of 7 micrograms per gram of sample. The water vapor pressures were measured with a 100 mm Barocol (Datametrics, Inc.) capacitive differential manometer sensor and associated electronics enabling accurate readings to better than 10<sup>-3</sup> mm.

## Ultraviolet Analysis of Aqueous Solutions

A Beckman DU spectrophotometer equipped with 1 cm matched quartz cells was used for the analysis of aqueous solutions of RDX. A stock solution of RDX (40 ppm) was prepared by dissolving 40 mg of recrystallized RDX (HMX-free) in 1 liter of distilled water. Aliquots of the stock solution were taken to prepare 1 to 10 ppm inclusively of standard RDX solutions. The absorbances of these standard solutions were measured on the spectrophotometer at 234 nm against a distilled water blank. The absorbances were plotted versus concentration, giving a linear plot. Unknown solutions were diluted to a concentration in the range of 1 to 10 ppm, the absorbances determined, and the appropriate dilution factor applied to give the concentration.

### Column Cycling (Adsorption-Desorption)

A 34 x 106 cm glass column with 19/22 joints at both ends was plugged just above the joint at the bottom end with glass wool. A "U" shaped siphon outlet was placed at this end of the column and the top end was fitted with a 1 liter funnel to hold stock RDX solution. The funnel was equipped with an overflow tube to allow excess solution to run back into the stock carboy (a 5-gallon polyethylene bottle). The solution was pumped to the funnel with a peristaltic pump timed to be activated 50% of the time, so as to maintain a constant head pressure ( $\Delta v = 60$  ml).

Four grams of GAC were weighed accurately into a 250 mL beaker and slurried with ca. 100 mL water. The slurry was poured into the funnel and allowed to settle in the column with the aid of gentle tapping and a stream of water where necessary. The prepared column was clamped in the center of an automatic 20 position fraction collector (Buchler Instruments, Fort Lee, NJ). The fraction collector was equipped with an activator to periodically advance an adjustable glass funnel so as to collect the eluent in 1 liter polyethylene bottles.

On-column cycling was carried out by monitoring the effluent for RDX concentration from the columns. The breakthrough point was set at an effluent concentration of 1 ppm. Loading the column with RDX was terminated as soon as the effluent reached this concentration. The amount of RDX adsorbed at 1 ppm effluent concentration was considered the capacity of the carbon. The specific adsorption of the column was calculated by dividing the total amount of RDX adsorbed by the weight of carbon in the column.

After breakthrough, the column was desorbed by adding 100 mL increments of solvent, starting with 20% acetone/water, followed by successive increments of 20% up to 100% acetone, and continued until approximately 1 liter of eluent was collected. The column was then washed with distilled water until all of the acetone was displaced (several 100 mL portions). After waterwashing, the column was ready for adsorption. The acetone extract was reserved for analysis.

The amount of RDX desorbed was determined by transferring the eluate to a 1 liter volumetric flask and diluting to the mark with acetone. A 10 mL aliquot was transferred to a 100 mL volumetric flask and diluted to the mark with water. A 10 mL aliquot was then transferred to a 250 mL beaker, diluted to 100 mL with distilled water, and evaporated on a hot plate to ca. 50 mL to remove acetone. The remaining aqueous solution was transferred quantitatively to a 100 mL volumetric flask, diluted to the mark, and the concentration determined by UV spectroscopy. The amount of RDX desorbed was calculated as follows:

$$\text{Amt. RDX, g} = \frac{1000}{10} \times \frac{100}{10} \times \frac{10}{100} = 0.1 \times C \quad (\text{where } C \text{ is in mg})$$

#### Batch Cycling (Adsorption-Desorption)

Fifty mg of GAC was accurately weighed into a glass stoppered, 1 liter Erlenmeyer flask, and 500 ml of a 30 ppm aqueous solution of RDX added. This ratio of carbon to volume of RDX stock solution was always used to insure adsorption at the plateau region of the adsorption isotherm. The charged flask was placed on a wrist-action shaker and shaken for 24 hours to attain equilibrium. The amount adsorbed by the carbon was determined by withdrawing an aliquot of supernatant solution from the flask and determining the concentration of RDX by UV spectroscopy. The concentration,  $C_1$ , was subtracted from the initial concentration,  $C_0$ , of RDX stock solution and the specific adsorption calculated by the following:

$$\text{Specific adsorption} = \frac{C_0 - C_1}{2m}$$

where:

- $m$  = weight of carbon, mg
- $2$  = correction factor for the volume of RDX solution used
- $C_0$  = initial concentration of RDX stock solution
- $C_1$  = equilibrium concentration

The RDX solution was carefully decanted from the carbon and the carbon rinsed once with a small quantity of water. Fifty mL of CP acetone were added to the flask, the stoppered flask was shaken for 1 hour, and the acetone was decanted into a 250 mL volumetric flask. The process was repeated two more times with the washings being added to the volumetric flask. After dilution to the mark, a 10 mL aliquot was pipetted into a 250 mL beaker containing approximately 75 mL of water, brought to a gentle boil on a hot plate, and evaporated to about 50 mL. This process expelled the acetone, giving a residual aqueous solution of RDX, which was diluted to volume (100 mL) in a volumetric flask. The concentration was determined by UV spectroscopy and the specific desorption calculated as follows:

$$\text{Specific desorption} = \frac{250}{10} \times \frac{100}{1000} \times \frac{C}{m} = 2.5 \frac{C}{m}$$

where:

- $m$  = weight of carbon (50 mg)
- $C$  = concentration of RDX, ppm

The entire operation was repeated for the next cycle using the eluted carbon remaining in the flask.

## RESULTS AND DISCUSSION

The RDX has a low solubility in water (approximately 50 ppm at 25°C), only about 1/3 of that of TNT. Since it is present in pink water along with TNT, consideration must be given to its interaction with GAC to remove it more efficiently from wastewaters.

As a general rule in adsorption from solution, less soluble solutes are more strongly adsorbed than the more soluble solutes. However, in the case of RDX versus TNT, where TNT is more soluble than RDX, TNT has a greater adsorption affinity than RDX. Evidence for this is presented in figure 1, which shows low concentration range isotherms on FS300 for both explosives where the specific adsorptions are plotted against the reduced concentration. The inflection of the isotherm for TNT is much sharper than that for RDX, indicating a higher energy of adsorption for the TNT. This higher adsorptivity and higher energy of adsorption is attributed to the aromatic nature of the TNT molecule as contrasted to the aliphatic nature of RDX. The TNT and RDX molecules contain three nitro groups each, which act as strong electron-withdrawing groups. The electron density in the  $\pi$  electron system of the aromatic TNT molecule is reduced, and the molecule acts as an acceptor in the complex formed with the carbon surface. This charge transfer complex is much stronger than the RDX-carbon complex. Thus, it appears that the nitro group is directly involved in the solute-carbon adsorption and that interaction of the aromatic ring with the carbon surface must enhance this reaction via the  $\pi$  electron system of the aromatic ring (TNT). Additional evidence for this type of mechanism is given by the work of DiGiano and Weber cited in reference 3. These researchers examined the adsorption from solution of 2,4-dinitrophenol and p-nitrophenol on active carbon and found that the dinitrophenol was adsorbed more strongly. There is an obviously larger electron withdrawal for two nitro groups as compared to one nitro group. Since the capacity and energy of adsorption for RDX is considerably less than that of TNT, it was expected that the degradation of the GAC with cycling would be less for RDX than for TNT.

However, as will be shown later, this is not necessarily the case. As mentioned in a previous report (ref 2), the initial approach towards improving the solvent regeneration of the GAC was to pacify the surface by preferentially reacting the high energy sites with certain molecules, which would then favor the reversible adsorption of TNT molecules. This rationale was also applied to RDX, and hence, the ensuing study of the interaction of RDX with the pretreated GAC's used with TNT.

### Surface Area Degradation

The same technique was used to evaluate the GAC's for RDX cycling as was used for TNT. The batch cycling experiments give the equilibrium concentration of RDX at the plateau of the RDX isotherm, whereas the column cycling experiments are dynamic and do not refer to equilibrium conditions, but rather to the capacity of the column at the breakthrough point of 1 ppm. The degradation curves, which show the loss of capacity with cycling for batch and column, fit the mathematical model of second order chemical kinetics, and therefore, linear equations may be

obtained which give the rate of degradation and the adsorption capacity at zero cycles. Table 1 presents the values obtained from such treatment of the data, i.e., the rate constants or rates of degradation, the adsorption capacity,  $C_0$ , and from the integration of these linear equations, the areas under the curves have been obtained, which may be used to evaluate the carbons quantitatively. The carbons, which demonstrated an improvement in cycling characteristics over the standard FS300 virgin, were the same ones which were superior in reference 2, namely Witco 337, FS400, and FS300/H<sub>2</sub>. In addition, two of the pretreated carbons, FS300/CH<sub>4</sub> and FS300/NO, showed a small improvement, although this was not the case when cycled with TNT. Figure 2 presents the linear plots of the degradation curves for the column cycling experiments with the ordinate in terms of specific adsorption, and the slope of the rate curves changed to negative values so as to be more in accord with the concept of degradation. The order of these curves is the same as in table 1, namely the top curve is the one for Witco, the next for FS400, and so on. We can tentatively conclude that although the interaction of RDX with the surface of GAC appears to be less than that of TNT with the same carbon, the amount of degradation seems to be of the same order.

Table 2 compares the surface areas of the pretreated GAC's before cycling and after cycling for seven column cycles. The ratios of surface areas relative to the standard FS300 are listed for uncycled and cycled carbons. In general, the better uncycled carbons, e.g. Witco, FS400, FS300/H<sub>2</sub>, have a higher surface area ratio in roughly the same order as shown by the cycling experiments in table 1. The ratios after cycling are even more revealing in that the order is the same, but the ratios are larger, implying less relative loss of surface area for the carbons superior to FS300. The pretreatments have had the effect of decreasing the surface area of the FS300, except in the case of the hydrogen pretreatment. An interpretation of an increase in surface area by the hydrogen pretreatment is given in the section on adsorption-desorption isotherms.

The progressive decline in capacity with cycling in the case of TNT was attributed to the irreversible adsorption of TNT at pore mouths. In a like manner, the loss of capacity when cycling with RDX is attributed to the same type of irreversible adsorption. To establish this, the surface of GAC's with irreversibly adsorbed RDX was examined with ESCA. Figure 3 presents the electron spectrum of neat RDX, which shows two strong peaks for nitro nitrogen and amine nitrogen. Figure 4 shows an electron spectrum of the RDX/carbon surface complex residue after it was exhaustively desorbed with acetone. In addition to the two peaks attributed to nitro and amine nitrogens, there is much structure attributed to reduced oxidative states of nitrogen, one form of which is identifiable as nitroso nitrogen. These results are evidence of a chemical reaction of RDX with the surface of the carbon, probably at the active sites of the pore mouths. As mentioned before, it has been postulated that much of the irreversible adsorption of the TNT molecule could be attributed to  $\pi$ - $\pi$  bonding as well as to  $-NO_2$  charge transfer at the pore openings and because of this buildup with cycling, the porous structure progressively becomes occluded. Although the adsorbitivity and the amount of RDX adsorbed is less than that of TNT, the decline in capacity with RDX cycling is relatively large. Thus, in much the same way as with TNT, there is a progressive loss of surface area with cycling. The RDX/carbon complex formulation may be attributed to the interaction of nitro groups of RDX with the reducing carbon surface, especially at the pore mouths.

## Adsorption/Desorption Isotherms

To further examine the porous structure of the GAC's as a function of cycling and hence degradation, water adsorption/desorption isotherms were used. If a change in the structure of the pores has taken place, e.g., a narrowing of the pore openings due to irreversible adsorption, the shape and wideness of the hysteresis loop will give a semiquantitative picture of the narrowing. A common model of a pore is the "ink bottle," one where the opening into the ink bottle is very narrow as compared to the wide body.

In general, adsorption on GAC's up to a relative pressure of 0.4 is due to the presence of polar or high energy sites on carbon. Water molecules adsorb at these sites and act as secondary adsorption sites, which by means of hydrogen bonding adsorb other water molecules. This type of adsorption can take place on the external surface within the pores, or in the pore openings.

Figure 5 presents the low pressure isotherms for water on FS300/virgin FS300/6 cycle (RDX), WITCO/virgin, and WITCO/6 cycle where the adsorbed water is expressed in units of water molecules per  $100\text{\AA}^2$ . Since water has a cross-sectional area of  $10\text{\AA}^2$  per molecule, a statistical monolayer occurs when the amount adsorbed is 10 molecules per  $100\text{\AA}^2$ . The results in figure 5 show that all the charcoal samples are relatively hydrophobic. Both the FS300 and WITCO 337 virgin charcoals are very similar in their degree of hydrophobicity. The surprising result, however, is that after six cycles of RDX exposure, the WITCO 337 becomes more hydrophobic, while the FS300 becomes more hydrophilic. The interpretation is that the chemi- and strongly adsorbed RDX is essentially hydrophilic, and that therefore, there is more chemi- and strongly adsorbed RDX left on FS300 than on the WITCO 337 after solvent regeneration. The difference also may be due to the fact that WITCO is manufactured from a petroleum based stock and FS300 from bituminous coal.

The steep rise in the adsorption isotherm curve in the higher relative pressure region is associated with condensation in the pores which is related to the pore diameters as described by the Kelvin equation. The pressure on the adsorption side of the hysteresis loop is in equilibrium with menisci in the body of the pores, and therefore gives information about the pore body diameters. During the course of desorption, the pressure is in equilibrium with menisci at the narrow pore mouths, and gives information about the pore mouth diameters. The hysteresis loop yields information concerning the size, shape, and uniformity of the pores. The more vertical the adsorption and desorption legs of the loop are, the more uniform in size are the pores.

Pore size analyses from water adsorption/desorption isotherms of the various samples of carbon were carried out using FS300 as the standard for comparison. Changes in pore size distributions are graphically set forth in figures 6 through 15. For a given carbon pore body or pore opening diameter, the amount of water adsorbed is shown on the ordinate as the positive or negative difference from the amount of water adsorbed on FS300. A positive number shows a higher concentration of that pore, size and conversely, a negative number shows a lower concentration of that pore size than the same size pore in the FS300.

Figure 6 shows the relative changes in pore opening diameter of FS300/1 cycle/RDX and FS300/6 cycle/RDX. A progressive shift to a higher concentration of pore openings in the 20 to 30Å diameter range is observed, and a marked shift to a lower concentration of pore openings in the range above 30Å is shown to take place with cycling. The pore body plots (fig. 7) shows a similar trend where a higher concentration of pore bodies occurs in the 20 to 35Å range, and a lower concentration in the higher size pore bodies due to progressive filling of the pore bodies.

Figure 8 depicts the pore opening diameters of virgin and cycled FS400 relative to FS300. FS400 has a higher concentration of pore opening diameters in the range from 20 to 80Å. After seven cycles, there is an increase in the concentration of pore openings in the 20 to 35Å diameter range, and a small decrease in the concentration of pore openings in the 20 to 35Å diameter range. This pattern is repeated as shown in figure 9 where the pore body diameter concentration in the 20 to 80Å range is greater for the virgin FS400. After cycling there is the usual increase in the concentration of pore bodies in the 20 to 35Å diameter range and a gradual decrease in the concentration of pore bodies in the 35 to 80Å range, where even with the decrease after seven cycles, the concentration of pore bodies above 50Å is similar to those of virgin FS300.

Figure 10 shows the pore opening diameters of FS300/H<sub>2</sub> before and after seven cycles. A marked increase in the concentration of pore openings in the range 20 to 30Å after cycling is observed, together with a decrease in concentration of pore openings above 36Å. There is a decrease in the concentration of the small pore openings and a slight increase in the concentration of the larger pore openings as a result of the hydrogen treatment, and in the case of the pore body diameter (fig. 11), the FS300/H<sub>2</sub> before cycling showed a loss of concentration from 20 to 80Å, after cycling there is the usual gain in concentration of pore diameters in the smaller diameters and loss of concentration of pores above 57Å. Its superior cycling characteristics then must be attributed to the larger pore mouth openings, and an increase in pore body diameters above 80Å.

The GAC with the best cycling performance in this series, WITCO 337 (fig. 12), shows a pore opening diameter concentration slightly different than does the FS300 in the range 20 to 35Å, but with pore opening diameters in the range above 35Å at a much higher concentration. With cycling there is the usual growth in the concentration of pore opening diameters in the lower range of 20 to 35Å, and a decrease in concentration in the range above 35Å.

In the case of the pore body diameters (fig. 13), virgin WITCO shows a lower concentration of pore bodies in the range below 52Å. After one cycle there appears to be an anomaly, namely a growth in the number of pores with pore body diameters in the range between 20 to 80Å. Since a growth in concentration of these pores can only take place at the expense of larger pore bodies, it can be postulated that the virgin WITCO has a higher concentration of pores over 80Å in diameter and that irreversible adsorption has narrowed a significant proportion of them. With continued cycling, the number of pore body diameters between 20 and 80Å is diminished. As mentioned before, WITCO is derived from a petroleum stock, and its pore shapes may be different from carbons derived from a coal base such as those of the FS300 series.



The pore opening (fig. 14) and pore body diameter (fig. 15) distributions of FS300/NO and FS300/CH<sub>4</sub> are quite similar to those of cycled FS300; that is, RDX cycling results in an increase in the relative concentration of pores in the 25 to 35Å range and a decrease in the concentration of pores above 35Å. Since both these carbons were slightly superior to FS300 in their cycling properties, this trend can be attributed to a smaller loss of pores above 35Å, which can be seen by comparing figures 14 and 15 with figures 6 and 7.

This smaller decrease in the concentration of pore opening diameters and pore body diameters above 35Å with cycling can probably be attributed to the passivation of the carbon with the small chemisorbed CH<sub>4</sub> and NO molecules tending to make the build-up of the RDX chemisorbed moiety smaller than with the standard FS300. Thus, it is conceivable that a superior carbon for solvent regeneration could be developed by the proper selection of pore concentrations and selected passivation treatments.

Some additional insight into the reasons for the improved cycling behavior of FS400 and WITCO 337 may be seen in table 3, where the number of molecules of RDX adsorbed are reported on a unit surface area basis. The WITCO and FS400 have adsorbed a larger number of RDX molecules. This can be attributed to easier access of the RDX molecules through wider pore mouths to the surfaces of the pores, whereas with the FS300 it can be postulated that some of the pore surface area is not available to the RDX molecule because of smaller pore mouth diameters.

#### CONCLUSIONS

It has been shown that TNT and RDX chemisorb at the active sites on the activated carbon surface. The reaction of TNT is via  $\pi$ - $\pi$  bonding, as well as via -NO<sub>2</sub> charge transfer, forming complexes at the surface which build up with adsorption-solvent desorption cycling, leading to a progressive loss of surface. The reaction of RDX is limited to -NO<sub>2</sub> charge transfer, also leading to a progressive loss of surface.

Some of the pretreatments have drastically altered the pore size distribution and led to a marked loss of surface area. On the other hand, hydrogen treatment led to an improved carbon by altering the pore structure. It was found that in agreement with the previous study with TNT (ref 2), carbons which showed superior cycling properties had increased relative concentrations of pore diameters in the range from 50 to 100Å, and a higher ratio of pore opening diameters to pore body diameters.

Although pretreatment of the carbon with small molecules to passivate the surface has not led to more efficient solvent regeneration, it is conceivable that in conjunction with a proper pore size distribution, truly efficient carbons for solvent regeneration could be found. Accordingly, a screening of commercially available GAC's with properly selected pore size distributions should be carried out to select the most suitable ones for an efficient solvent regeneration process.

#### REFERENCES

1. T.C. Castorina, J. Haberman, and J. Sharma, "Charcoal Regeneration, Part I; Mechanism of TNT Adsorption," Technical Report ARLCD-TR-77065, ARRADCOM, Dover, New Jersey, November 1977.
2. F.J. Haberman, T.C. Castorina, S. Semel, and H. Kramer, "Charcoal Regeneration, Part II; Modified Carbon Surface Activity and Reversibility of TNT Adsorption," Technical Report ARLCD-TR-80012, ARRADCOM, Dover, New Jersey, July 1980.
3. J.S. Mattson and H.B. Mark, Jr., "Activated Carbon," Marcel Dekker, Inc., New York, 1971, p 221.

Table 1. Rates of degradation of pretreated carbons and integrated areas under the degradation curve

<u>Treatment</u>	<u>BATCH</u>		<u>Correlation coefficient</u>	<u>Area X 10<sup>-3</sup></u>
	<u>Rate constant</u>	<u>Co</u>		
FS300 (Virgin)	0.282	0.19	0.91	27
Methane at 700°C	0.261	0.22	0.92	32
Hydrogen at 1000°C	0.487	0.23	0.90	29
NO <sub>2</sub>	0.443	0.12	0.75	17
NO	0.459	0.19	0.73	26
FS400	0.265	0.22	0.82	31
WITCO 337	0.232	0.21	0.64	31

<u>COLUMN</u>				
FS300 (Virgin)	1.312	0.18	0.88	28
Methane at 700°C	0.513	0.22	0.94	27
Hydrogen at 1000°C	0.455	0.23	0.92	29
NO <sub>2</sub>	2.551	0.11	0.93	10
NO	0.497	0.14	0.77	20
FS400	0.479	0.24	0.93	30
WITCO 337	0.326	0.27	0.83	36

Table 2. Surface areas of pretreated carbons

Carbons	Uncycled carbons		Cycled carbons	
	Surface Area $\text{m}^2/\text{g}$	Ratio to FS300	Surface Area $\text{m}^2/\text{g}$ after 7 cycles	FS300
FS300 (Virgin)	1026	1.000	618	1.000
FS300/ $\text{CH}_4$ /5 hrs/ 700°C	995	0.970	685	1.108
FS300/ $\text{H}_2$ /1000°C/ 4 hrs	1127	1.098	775	1.254
FS300/ $\text{NO}_2$ /72 hrs	628	0.612	600	0.971
FS300/ $\text{NO}$ /4 hrs/ $\text{H}_2\text{O}$	794	0.774	735	1.189
FS400	1119	1.091	835	1.351
WITCO 337	1311	1.278	918	1.485

Table 3. Relative amount of RDX absorbed on carbons

Carbon	Surface area $\text{M}^2/\text{g}$	Specific ads. at same equil.conc.	No. molecules ads. $\times 10^{17} / \text{M}^2$
FS300	1026	0.302	1.457
FS400	1119	0.365	1.469
WITCO 337	1311	0.456	1.567

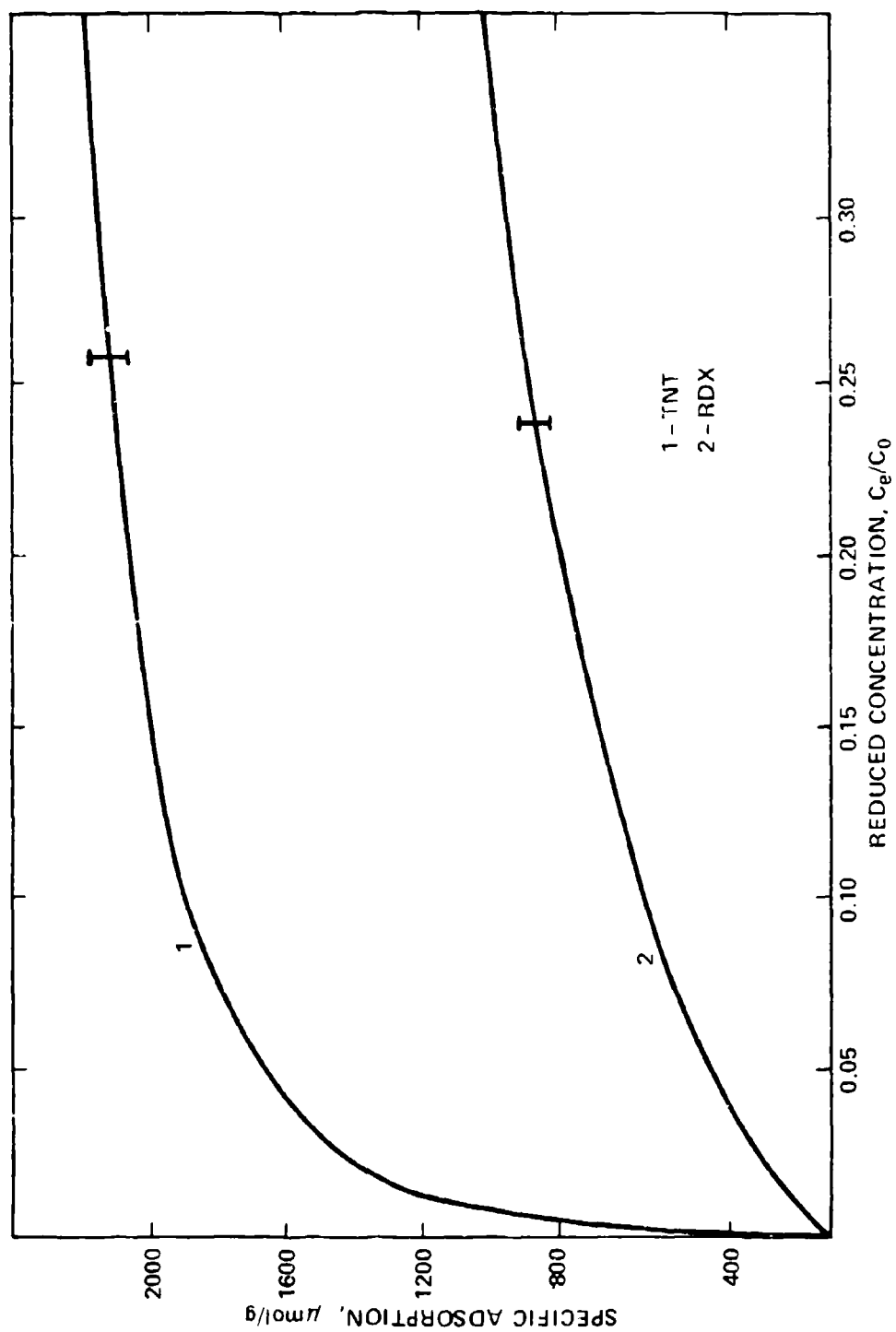


Figure 1. Adsorption isotherms of TNT and RDX on FS30G

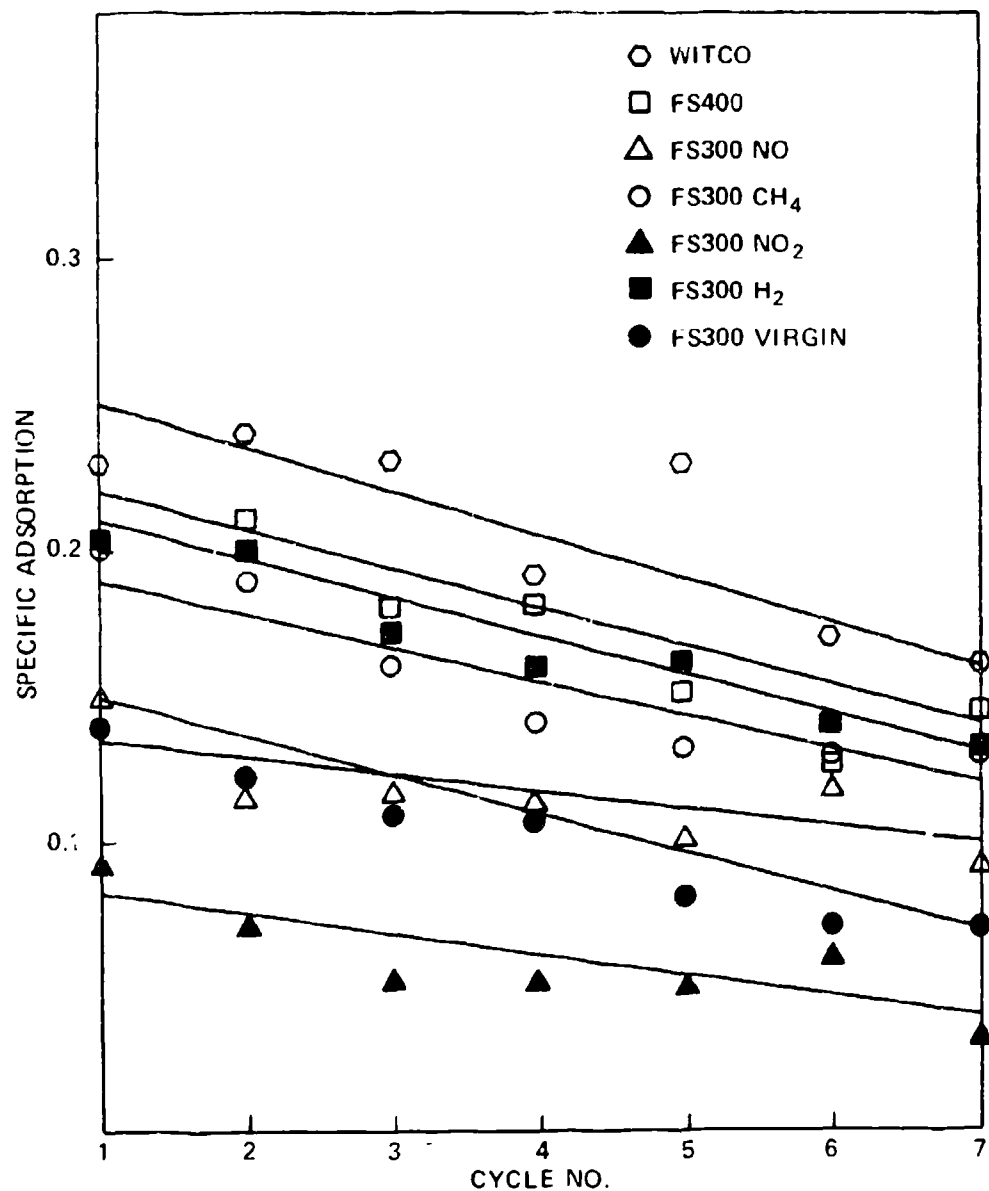


Figure 2. Linear plots of specific adsorption deactivation as a function of RDX adsorption/solvent desorption cycling according to a second order kinetic model

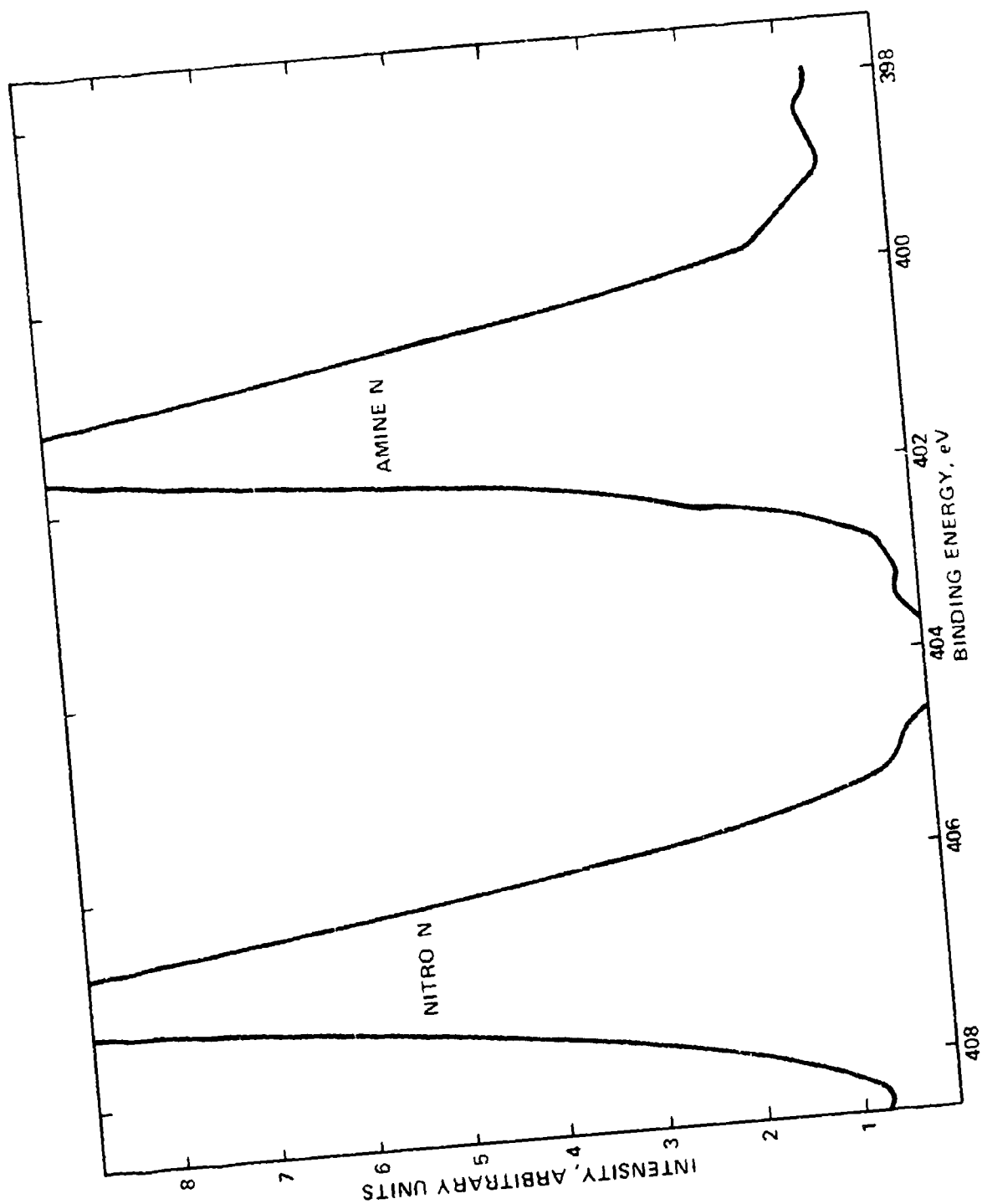


Figure 3. Electron spectrum of RDX

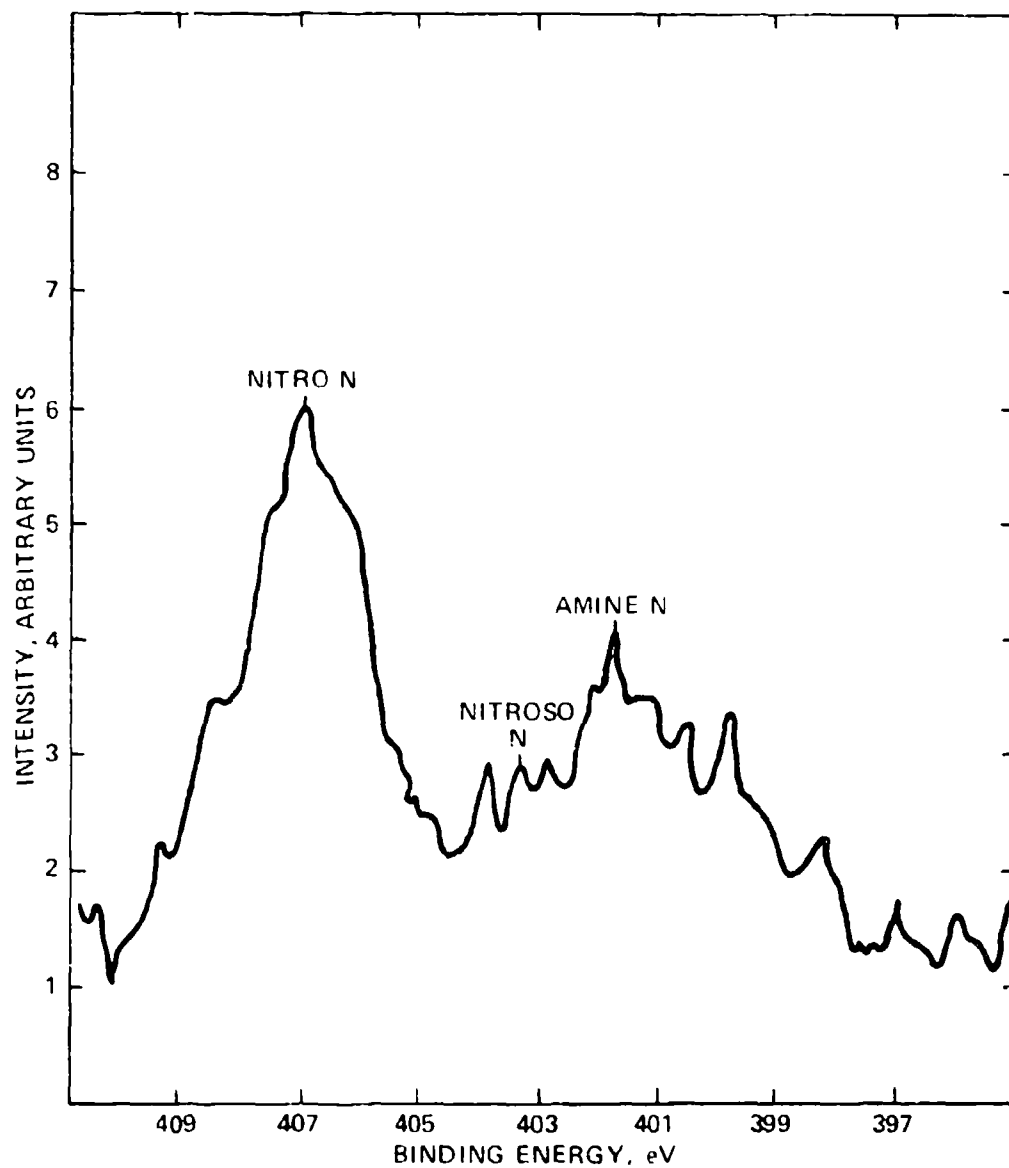


Figure 4. Electron spectrum of RDX/carbon surface complex



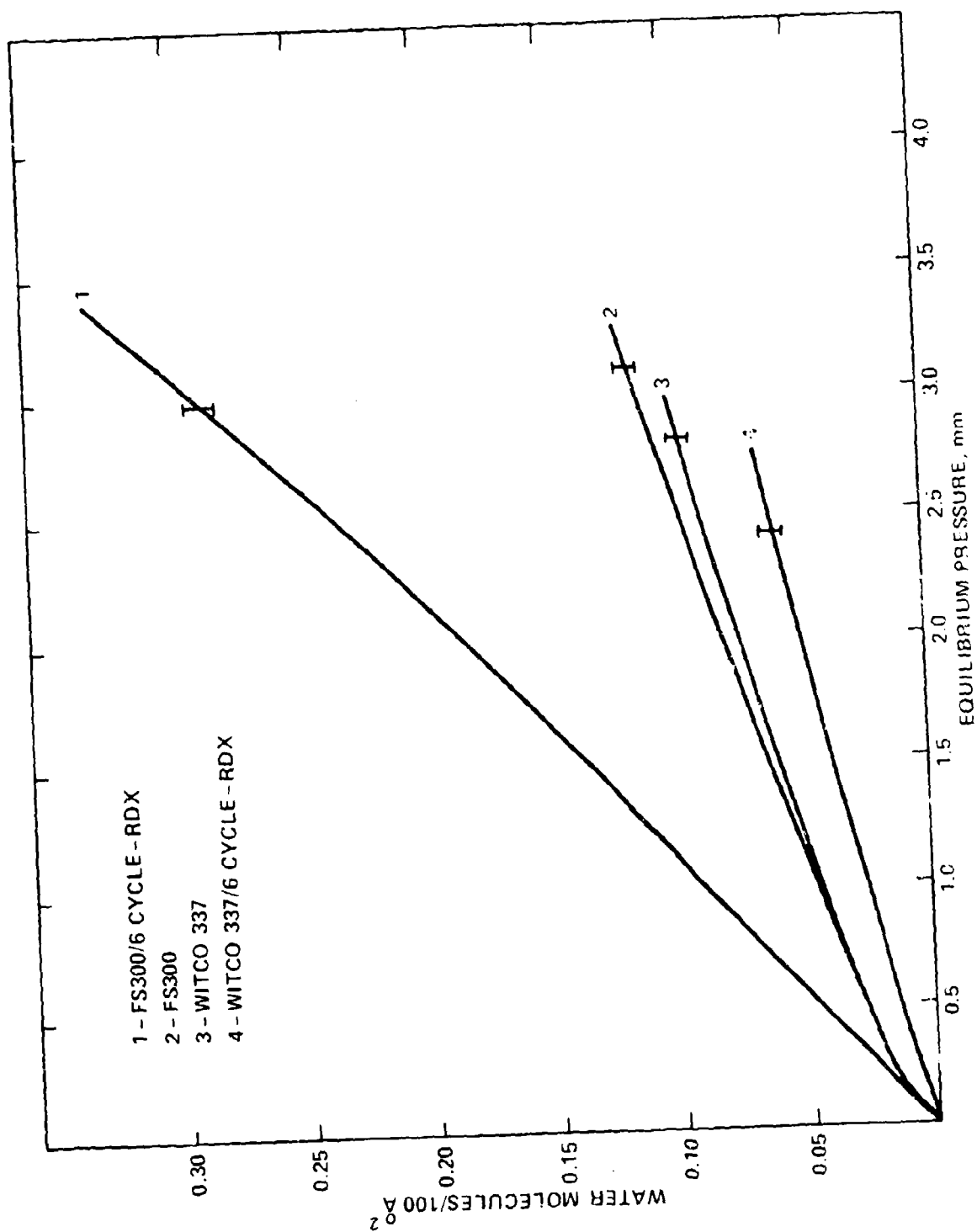


Figure 5. Low pressure water isotherms on some carbons

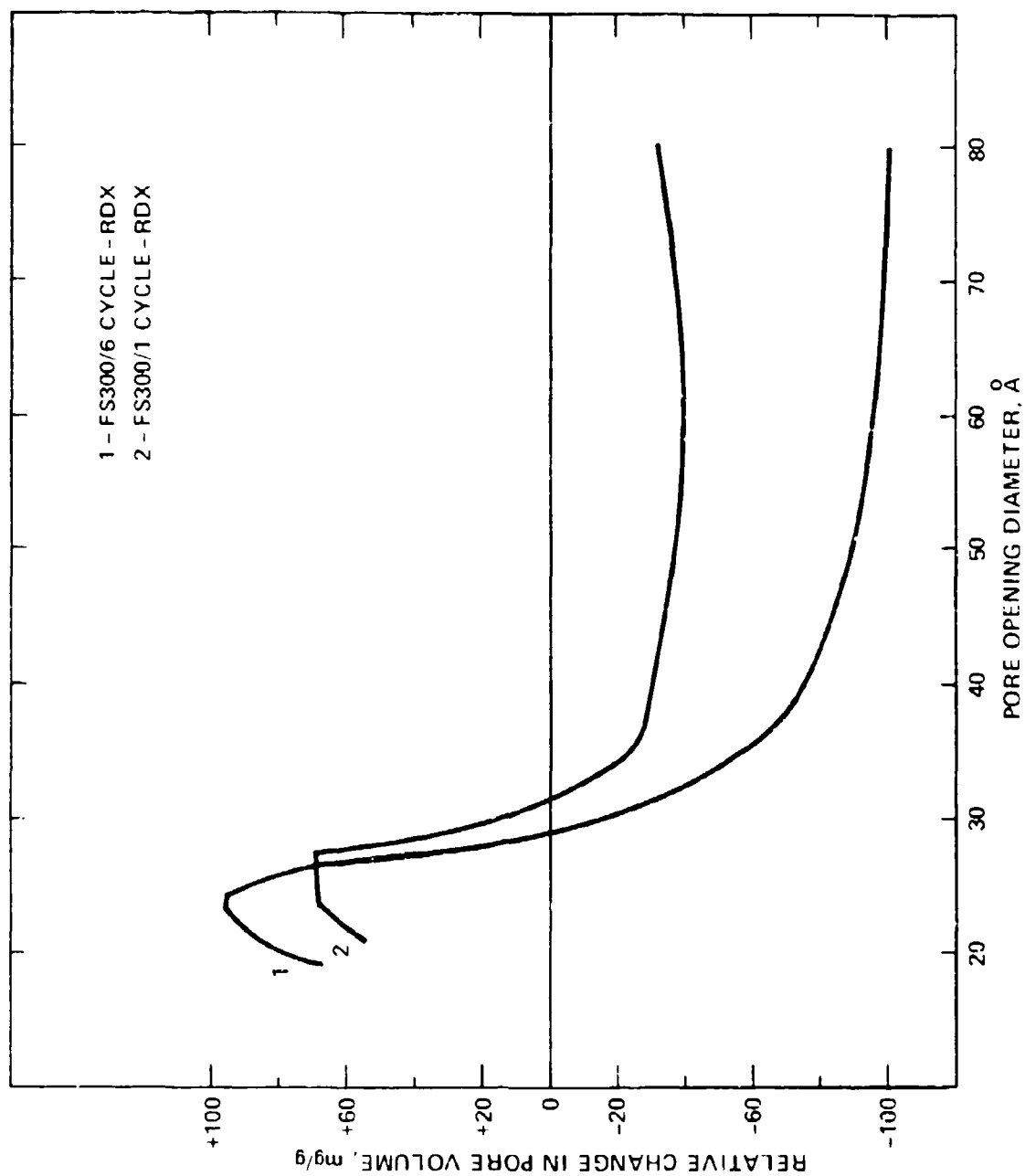


Figure 6. Change in pore opening size distribution relative to uncycled FS300 as a function of cycling

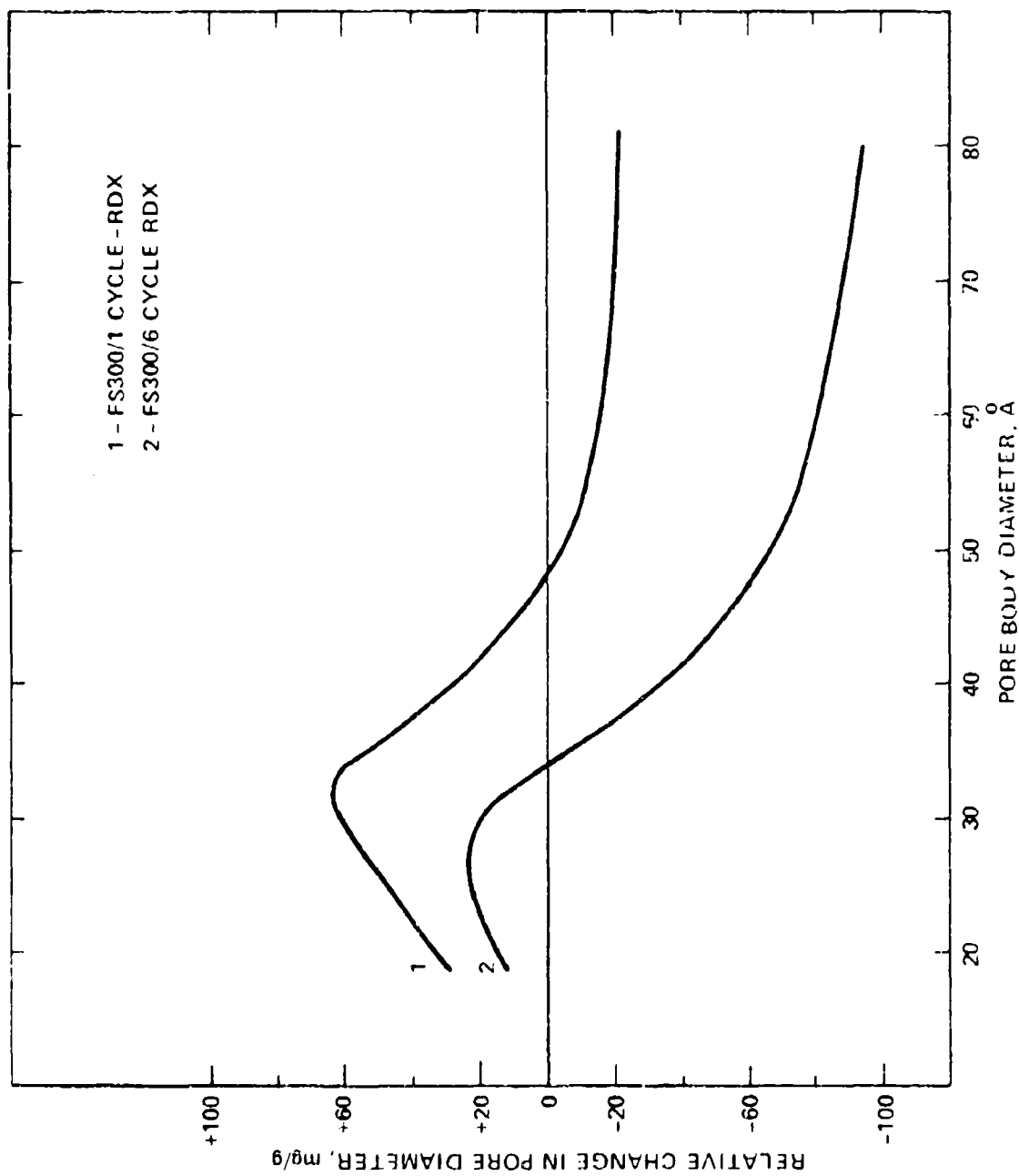


Figure 7. Change in pore body size distribution relative to uncycled FS300 as a function of cycling

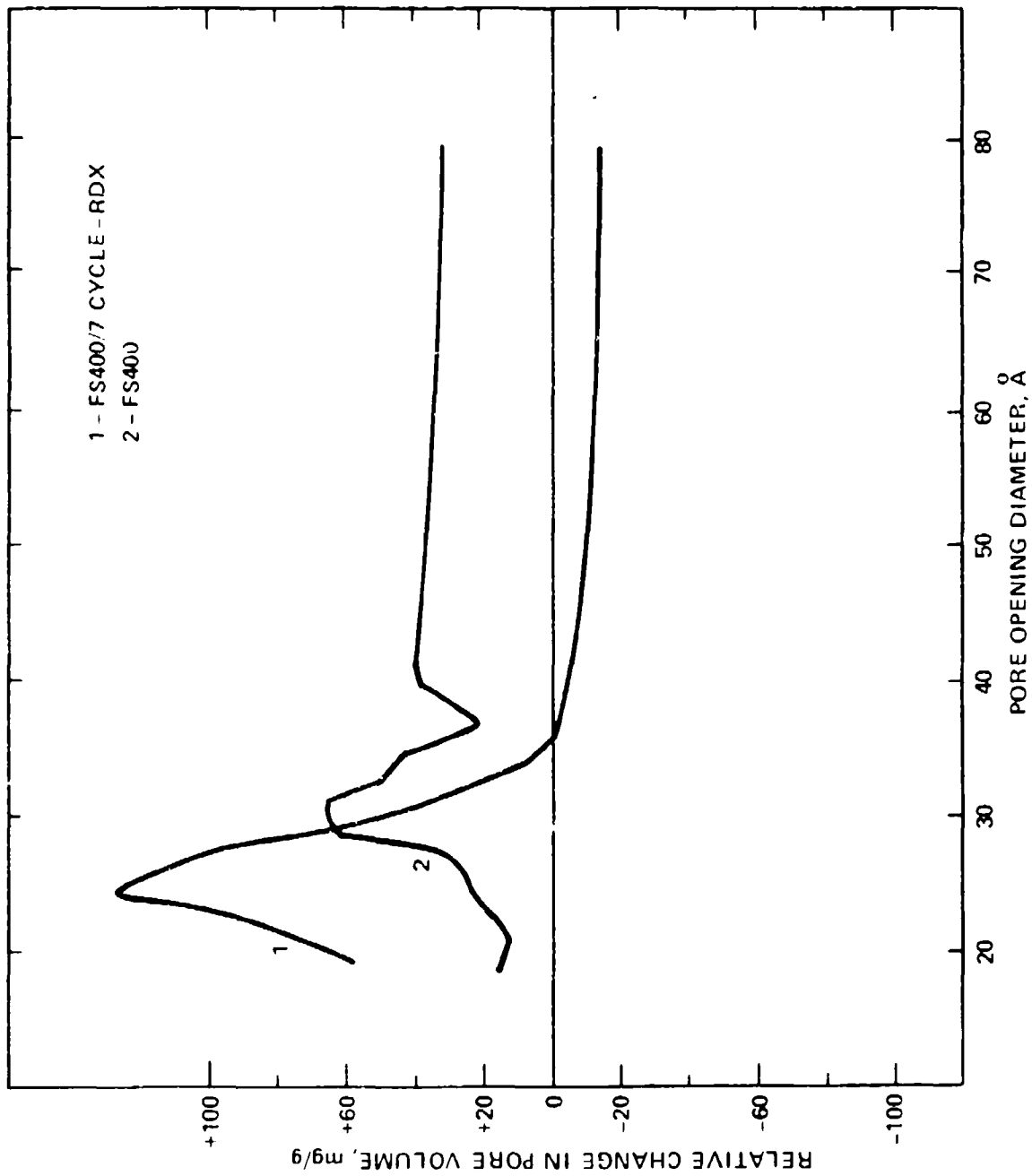


Figure 8. Change in pore opening size distribution relative to FS300 of RDX cycled FS400

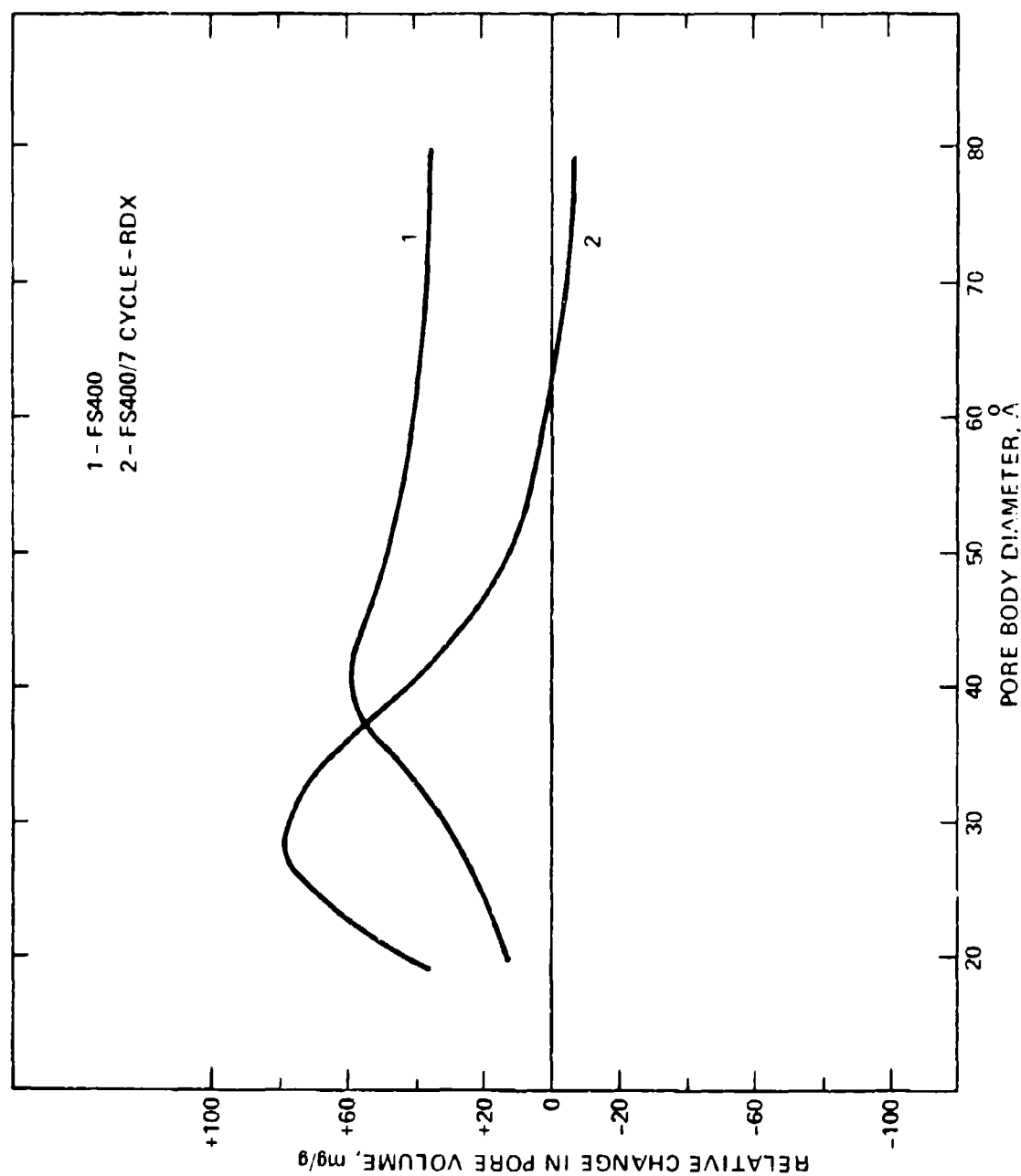


Figure 9. Change in pore body size distribution relative to FS300 of RDX cycled FS400

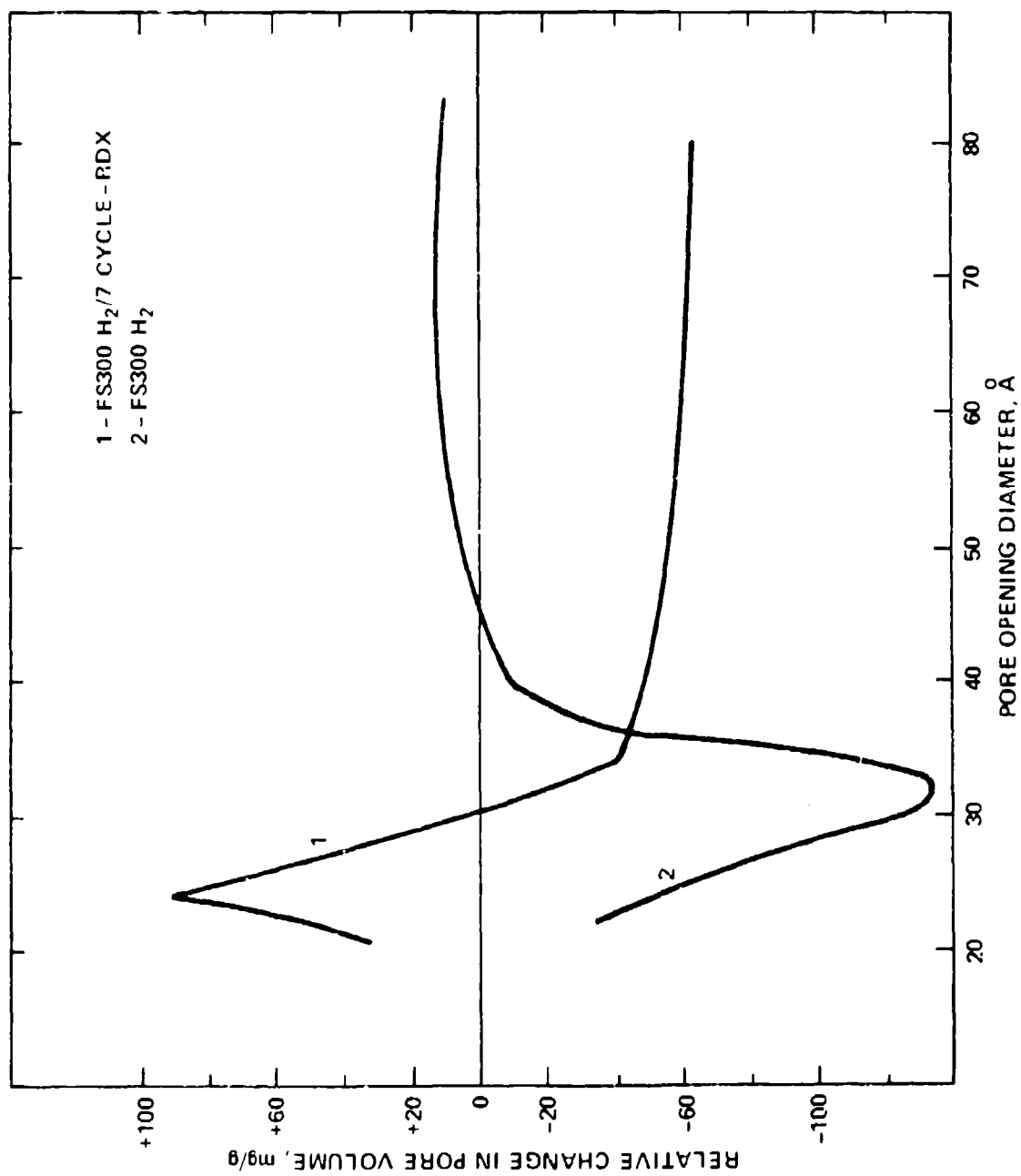


Figure 10. Change in pore opening size distribution relative to FS300 of RDX cycled hydrogen treated FS300

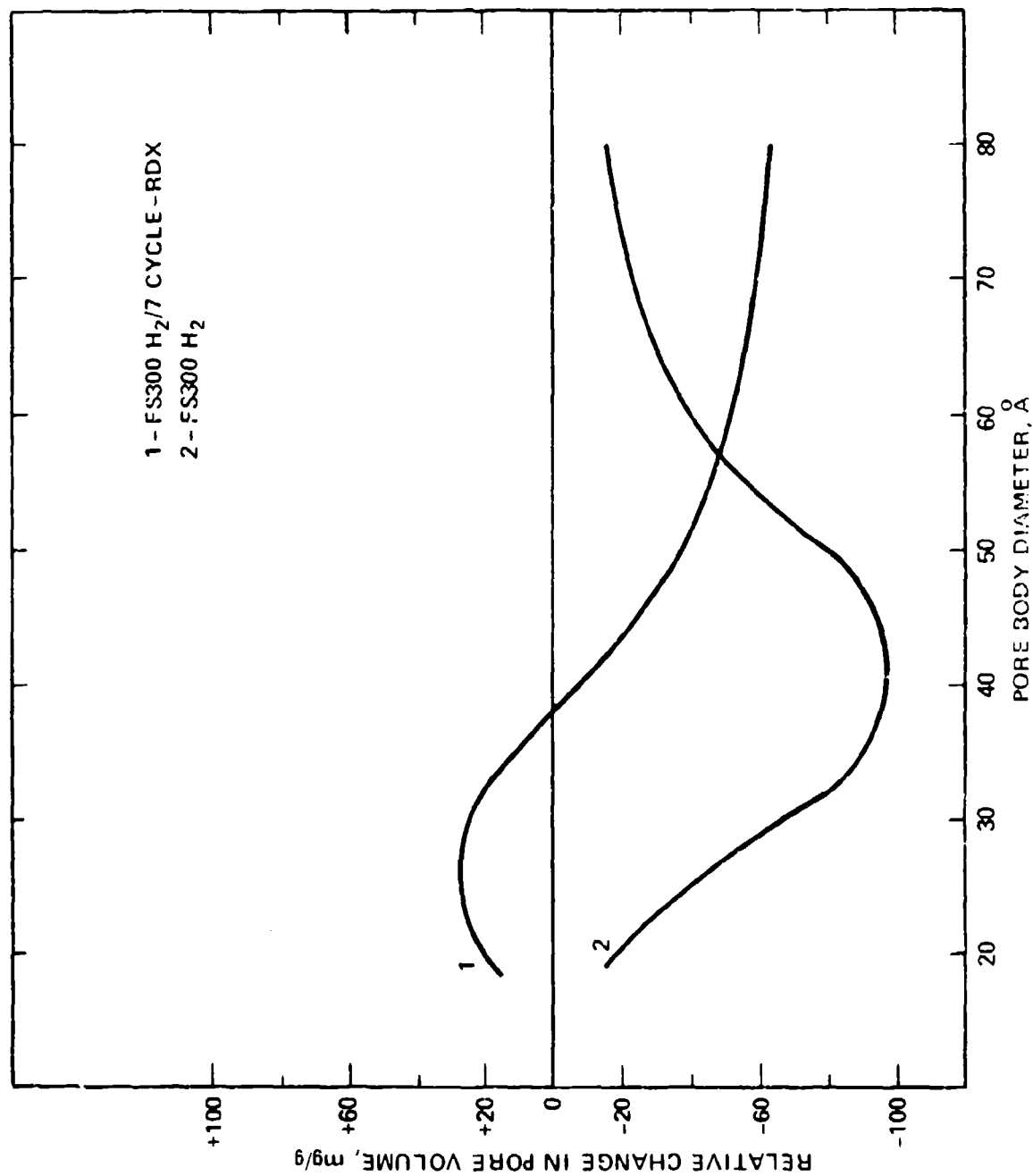


Figure 11. Change in pore body size distribution relative to FS300 of RDX cycled hydrogen treated FS300

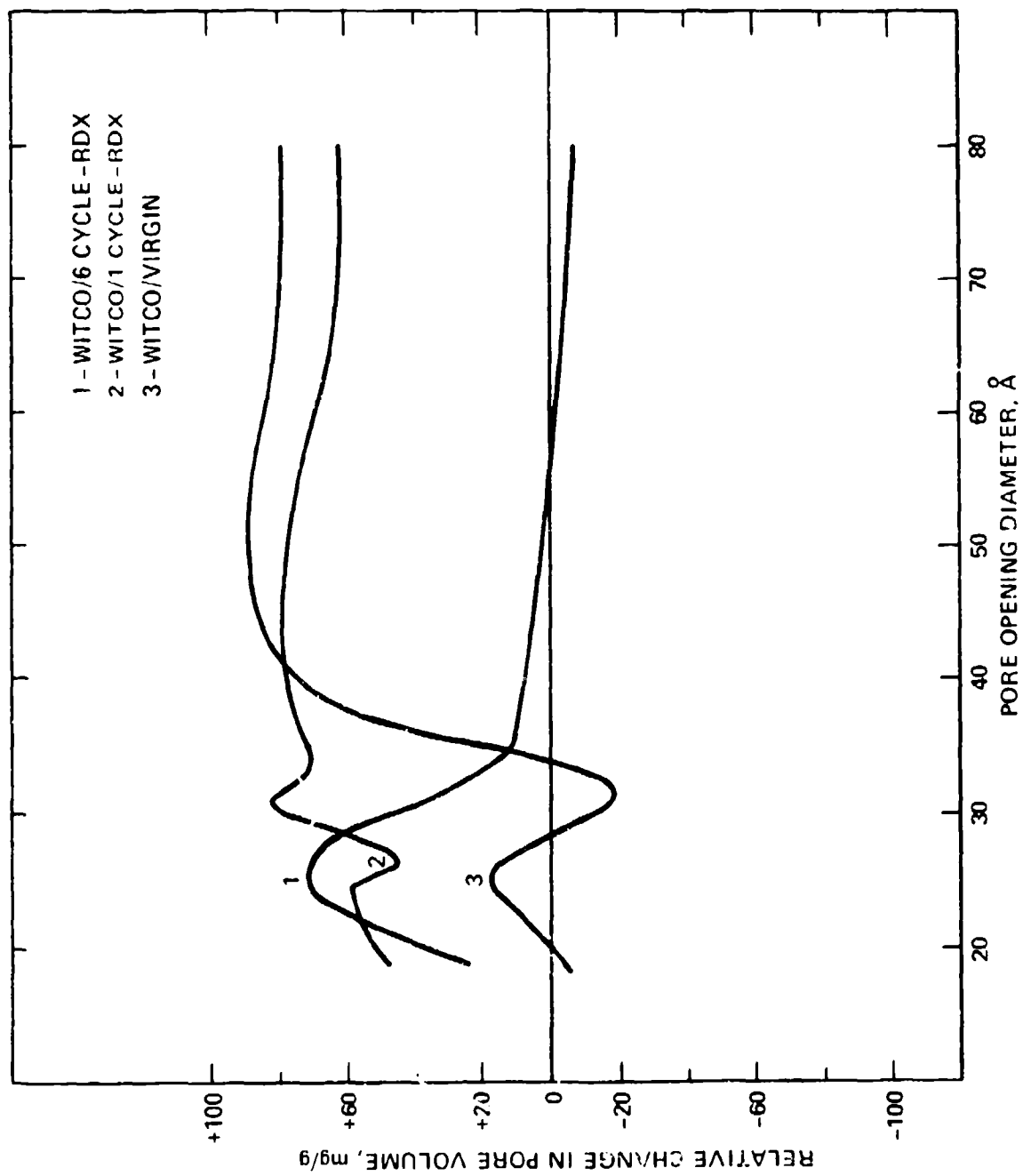


Figure 12. Change in pore opening size distribution relative to FS300 of RDX cycled WITCO carbon



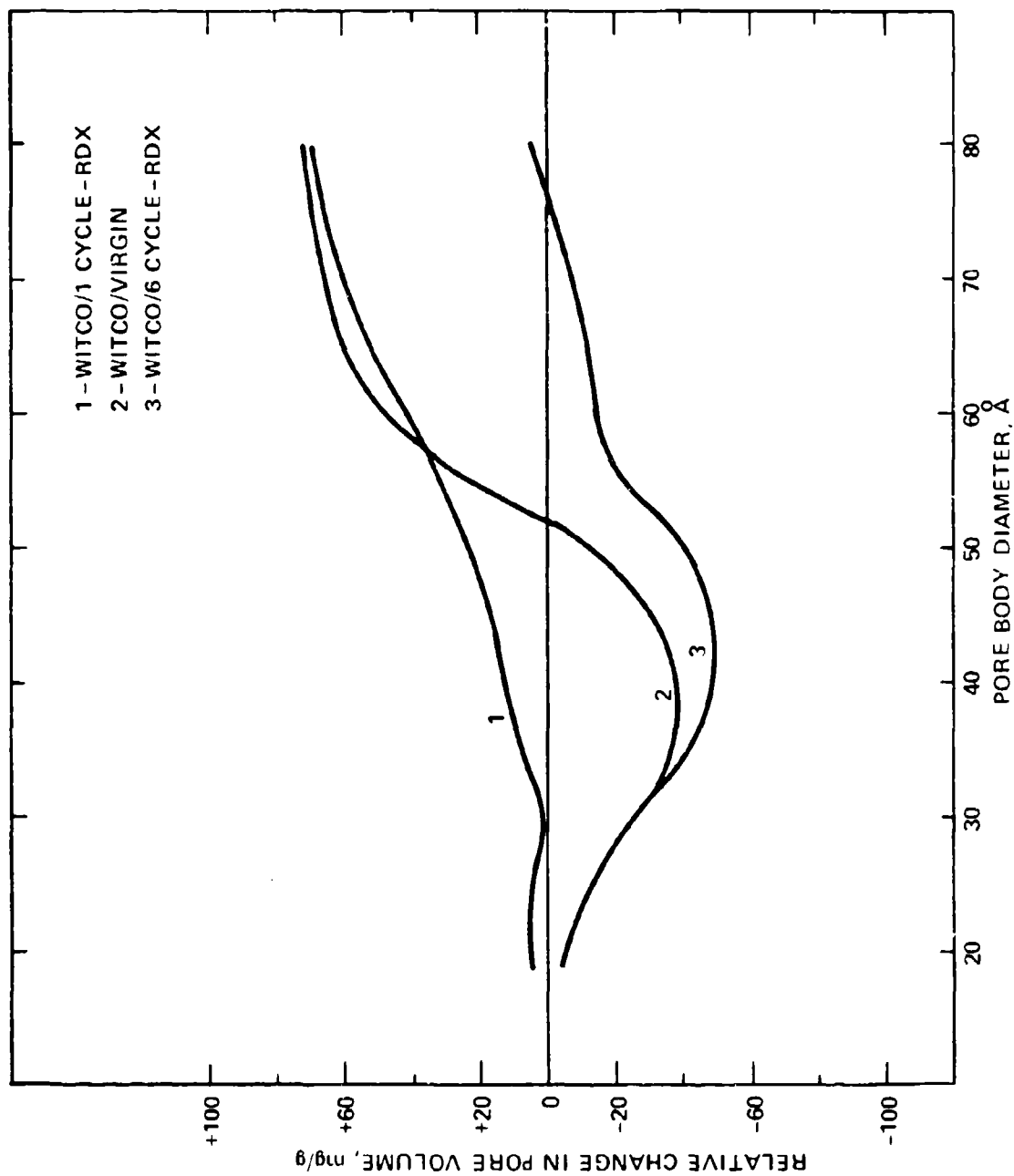


Figure 13. Change in pore body size distribution relative to FS300 of RDX cycled WITCO carbon

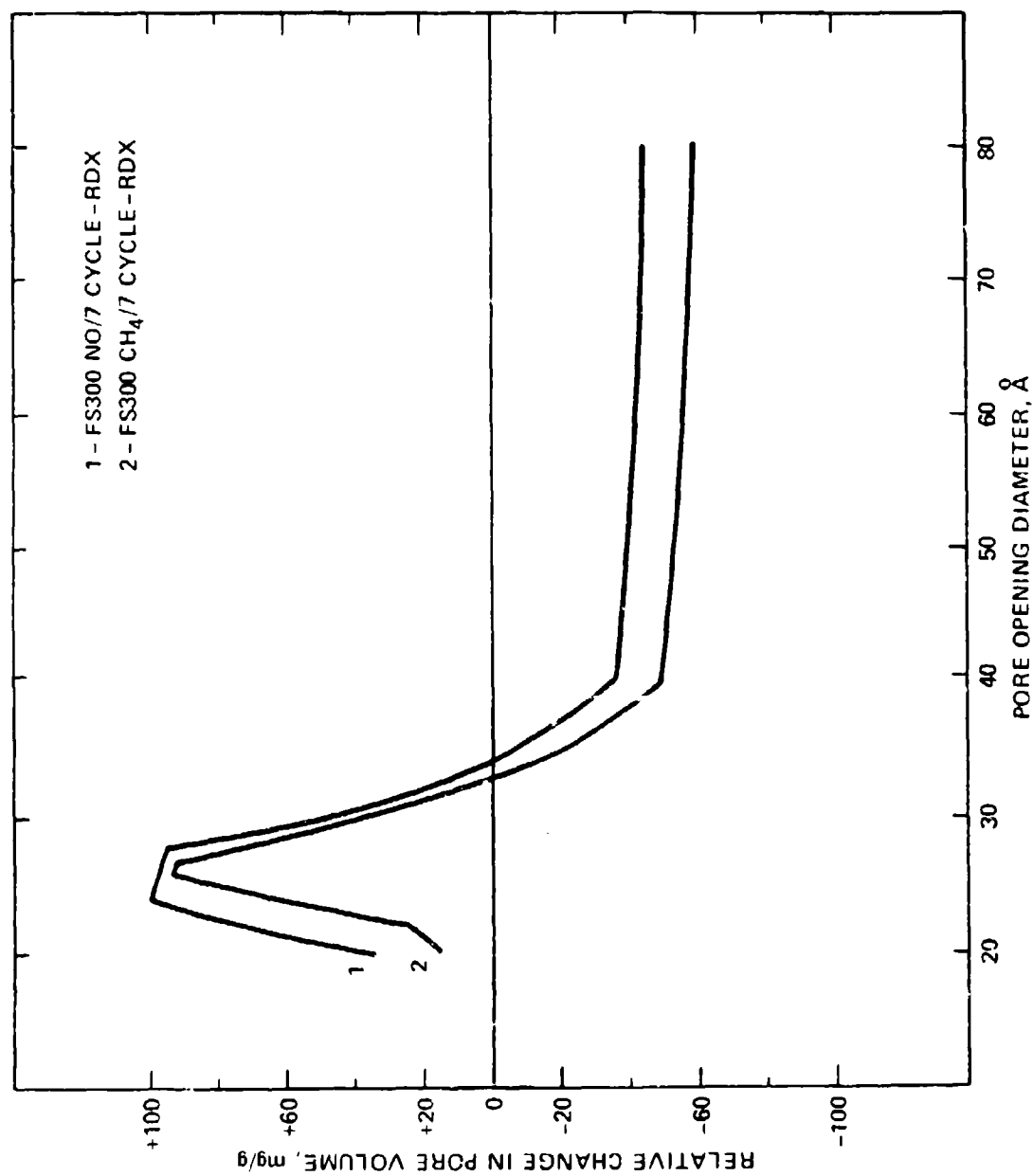


Figure 14. Change in pore opening size distribution relative to FS300 of NO and CH<sub>4</sub> treated FS300

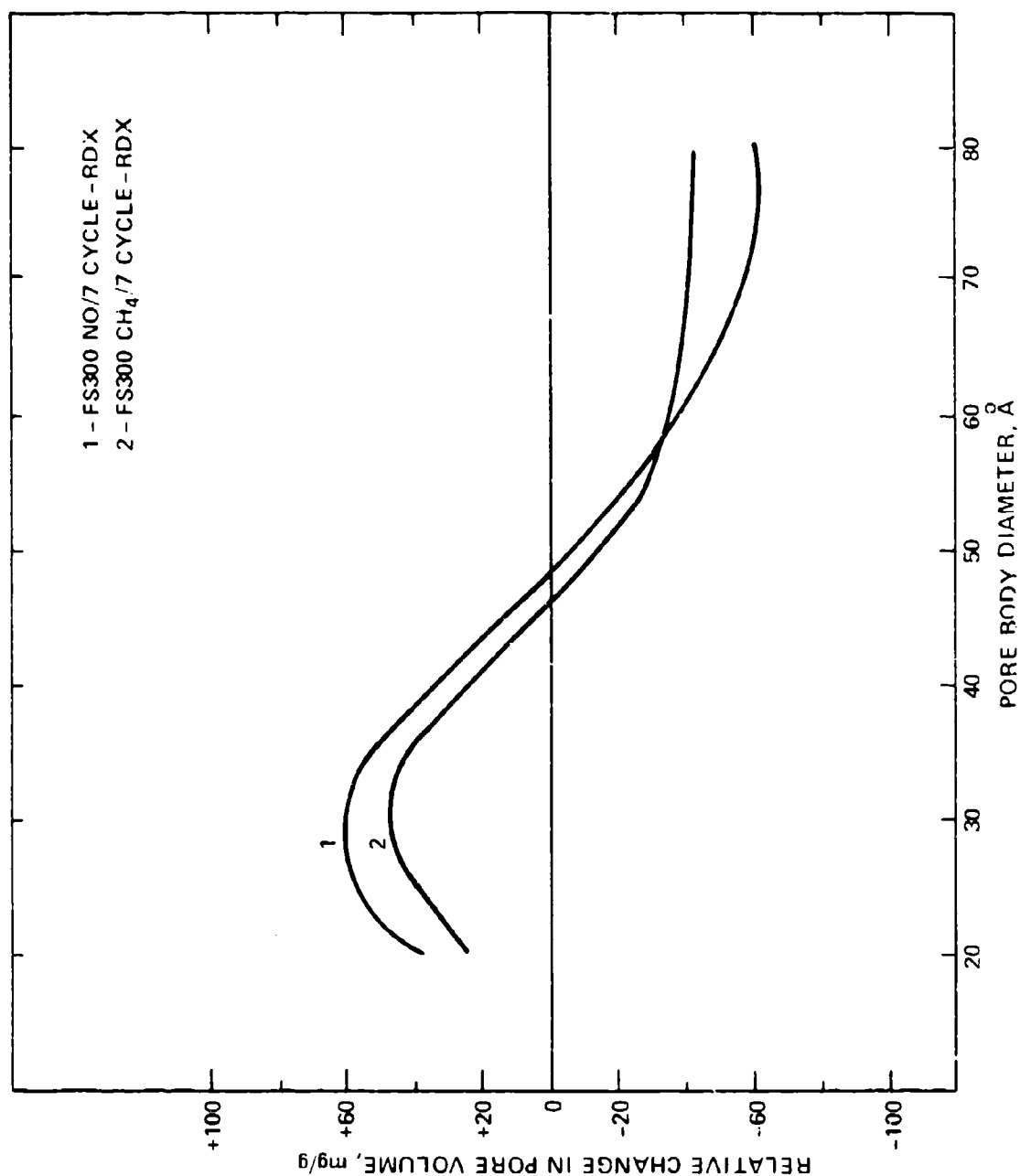


Figure 15. Change in pore body size distribution relative to FS300 of NO and CH<sub>4</sub> treated FS300

DISTRIBUTION LIST

Commander/Director  
U.S. Army Toxic and Hazardous Materials Agency  
ATTN: DRXTH-TE-D  
J.K. Bartel  
D. Renard (9)  
Aberdeen Proving Ground, MD 21010

Commander  
U.S. Army Armament R&D Command  
ATTN: DRDAR-CG, MG A.H. Light, Jr.  
DRDAR-GCL  
DRDAR-LC, COL R. Philipp  
DRDAR-LCE, Dr. R.F. Walker (3)  
DRDAR-LCE, Mr. J. Haberman (25)  
DRDAR-LCM, Mr. L. Saffian  
DRDAR-TD, Dr. R. Weigle  
DRDAR-TDS, Mr. V. Lindner  
DRDAR-TSS (5)  
Dover, NJ 07801

Commander  
Radford Army Ammunition Plant  
ATTN: Dr. W.T. Bolleter  
Hercules, Inc.  
Radford, VA 24241

Commander  
Badger Army Ammunition Plant  
Baraboo, WI 53913

Commander  
Indiana Army Ammunition Plant  
Charlestown, IN 47111

Commander  
Holston Army Ammunition Plant  
Kingsport, TN 37660

Administrator  
Defense Technical Information Center  
ATTN: Accessions Division (12)  
Cameron Station  
Alexandria, VA 22314

Commander  
Lone Star Army Ammunition Plant  
ATTN: Technical Library  
Texarkana, TX 75501

Commander  
Milan Army Ammunition Plant  
Milan, TN 38358

Commander  
Tooele Army Ammunition Plant  
Tooele, UT 84074

Commander  
Iowa Army Ammunition Plant  
Silas Mason, Mason & Hanger Inc.  
ATTN: Technical Library  
Middletown, IA 52638

Commander  
Joliet Army Ammunition Plant  
Joliet, IL 60436

Commander  
Longhorn Army Ammunition Plant  
Marshall, TX 75670

Commander  
Louisiana Army Ammunition Plant  
Shreveport, LA 71130

Commander  
Newport Army Ammunition Plant  
Newport, IN 47966

Commander  
Volunteer Army Ammunition Plant  
Chattanooga, TN 37401

Commander  
Kansas Army Ammunition Plant  
Parsons, KS 67357

Director  
U.S. Army Materiel Systems  
Analysis Activity  
ATTN: DRXSY-MP  
Aberdeen Proving Ground, MD 21005

Commander  
U.S. Army Research Office  
ATTN: Dr. G. Wyman  
Box CM, Duke Station  
Durham, NC 27706

Commander  
Naval Surface Weapon Center  
White Oak Laboratory  
ATTN: Technical Library  
Dr. J. Hoffsommer  
White Oak, Silver Spring, MD 20910

Director  
DARCOM Field Safety Activity  
ATTN: DRXOS-ES  
Charlestown, IN 47111

Commander  
U.S. Army Training & Doctrine Command  
ATTN: ATEN-ME  
Fort Monroe, VA 23651

Commander  
U.S. Naval Sea Systems Command  
ATTN: SEA-0332  
Dr. A.B. Amstar  
Washington, DC 20362

Lawrence Livermore Laboratory  
ATTN: Technical Library  
P.O. Box 808  
Livermore, CA 94550

Commander  
Fort Detrick  
U.S. Army Medical Bioengineering  
R&D Laboratory  
ATTN: Dr. D.H. Rosenblatt  
Frederick, MD 21701

Commander  
U.S. Army Armament Materiel  
Readiness Command  
ATTN: DRSAR-LEP-L  
Rock Island, IL 61299

Director  
U.S. Army TRADOC Systems Analysis  
Activity  
ATTN: ATAA-SL  
White Sands Missile Range, NM 88002

Director  
Ballistics Research Laboratory  
U.S. Army Armament Research and  
Development Command  
ATTN: DRDAR-TSB-S  
Aberdeen Proving Ground, MD 21005

Chief  
Benet Weapons Laboratory, LCWSL  
U.S. Army Armament Research and  
Development Command  
ATTN: DRDAR-LCB-TL  
Watervliet, NY 12189

Commander/Director  
Chemical Systems Laboratory  
U.S. Army Armament Research  
and Development Command  
ATTN: DRDAR-CLB-PA  
DRDAR-CLJ-L  
APG, Edgewood Area, MD 21010

Director  
Industrial Base Engineering Activity  
ATTN: DRXIB-MT  
Rock Island, IL 61299

$$-\beta_0^2 D^2 = -\beta^2 c^2 \quad (32)$$

We also have that the slope of the Hugoniot curves is

$$\left. \frac{\partial p}{\partial (1/\beta)} \right|_H = - \frac{\left[ \frac{1}{2} (p_1 + p_0) - \beta^2 \partial E / \partial \beta \right]}{\left[ \partial E / \partial \beta - \frac{1}{2} (1/\beta_0 - 1/\beta_1) \right]} \quad (33)$$

Combining Eqs. (27), (32), and (33), we get for the slope of the Hugoniot curves

$$\left. \frac{\partial p}{\partial (1/\beta)} \right|_H = -\beta^2 c^2 \quad (34)$$

Thus, the slope of the Rayleigh line is the same as the slope of the Hugoniot curve (which is determined by Eq. (31)) at the sonic locus. For the case where there is only one reaction Eq. (31) becomes  $R=0$  or  $\lambda=1$  at the sonic locus. This means that the one reaction is completed at the sonic locus. This justifies the CJ hypothesis which determines the Rayleigh line (and thus  $D$ ) by putting it tangent to the completed reaction Hugoniot. For the equation of state of Eq. (5), the above method yields that  $D$  satisfies

$$D^4 - 2D^2 c_0^2 \left[ 1 + \gamma \frac{\gamma^2 - 1}{c^2} \right] + c_0^4 = 0 \quad (35)$$

Eq. (35) has the two roots

$$D_{\pm}^2 = c_0^2 M_{\pm}^2 = c_0^2 \left\{ 1 + \gamma \frac{\gamma^2 - 1}{c^2} \pm \sqrt{\left[ 1 + \gamma \frac{\gamma^2 - 1}{c^2} \right]^2 - 1} \right\} \quad (36)$$



The two roots give two Rayleigh lines called  $R^+$  and  $R^-$ .  $R^+$  represents a CJ detonation while  $R^-$  represents a CJ deflagration. These are depicted in Fig. 2. For the CJ- solution the solution goes smoothly along  $R^-$  from the values at CJ- attained at the sonic locus. No shock takes place for this deflagration solution. For the detonation, the Von Neumann model is that the solution goes along the no reaction Hugoniot from O to N,  $p = p_1$  and  $\rho = \rho_1$  (with  $p_1$  and  $\rho_1$  determined from Eqs. (16) and (17) using Eq (36) for  $M_0$ ) and then down from N to CJ+ along  $R^+$ . A detonation solution going directly from

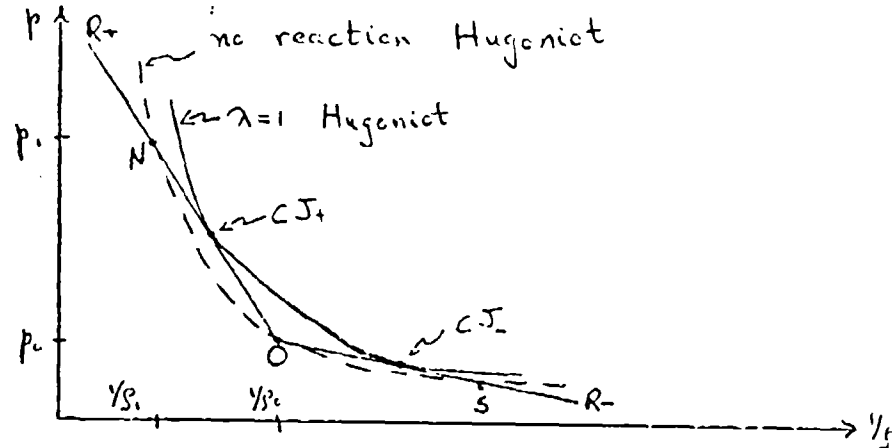


Fig. 2. The  $p - 1/\rho$  plane. CJ+ gives the pressure at the sonic locus for a detonation. CJ- gives the pressure for a deflagration

O to CJ+ along  $R^+$  with no shock is also allowed. Both solutions have the same final state CJ+ at the sonic locus and the same D. The no shock solution does not usually occur because of problems with initiating the reaction. The Von Neumann model in fact says that the O→CJ+ detonation is actually a mechanical shock to  $p_1$  followed by a deflagration from N to CJ+. Due to the way that the equations integrate through a shock, the point CJ+ is the same with or without a Von Neumann spike.

The CJ hypothesis is that the sonic locus is determined by tangency of the Rayleigh line to the completed reaction Hugoniot. If there are several irreversible exothermic reactions this hypothesis is correct (for 1-dimensional, steady flows). If some of the reactions are reversible, however, or if some of the  $\sigma_i$  may be negative as in mole decrement reactions, then Eq. (31) does not imply that the reactions are completed at the sonic locus.

Thus some of the chemical energy is released beyond it. This late energy is not effective in the detonation and nonideal behavior is found. The analysis of precisely what happens involves a study of the phase plane of Eq. (25). Many complicated results are possible depending on the details of the  $\sigma_i$  and the  $R_i$ . A fairly thorough discussion of the possibilities can be found in chapter 5 of Ref. 6, and in Wood and Salsburg<sup>10</sup>.

This brief discussion of steady, 1-dimensional detonations does not cover the entire subject. In this research effort we have made no contribution to this part of the field. There are good analytical methods, that supplemented by computer calculations, can predict the nonideal performance of steady, 1-dimensional detonations. An input to these methods, however, must contain a realistic description of the reaction kinetics. This is presently not known for most gaseous explosives, let alone solid ones. In the case of solid explosives, beyond the lack of information concerning the equation of state and the reaction kinetics, there are also the problems associated with inhomogeneous mixtures. Here the effects due to grain burning and diffusion of reactants are not fully worked out.

## V. DIVERGENT FLOW AND DETONATION FAILURE

When  $\omega$  is not negligible, Eqs. (8)-(12) need to be complemented by a way to compute  $\frac{\partial \omega}{\partial r}$  as a function of  $Z$ . This depends on the shape of the exploding charge and on the properties of the confining media. In general, to compute  $\omega$  one must solve a difficult free boundary problem with matching at the boundary to account for the properties of the different media. Even if  $\omega$  were known, however, there are still some interesting difficulties in integrating Eqs. (8)-(12). These equations should predict the observed phenomenon of detonation failure when the diameter of the exploding cylinder is small. We will cast those equations in the form for flow in a nozzle by letting

$$\frac{1}{A} \frac{dA}{dz} = \frac{2}{u} \frac{\partial \omega}{\partial r} \quad , \quad (37)$$

where  $A$  is the area of the nozzle. The equations become

$$\frac{d}{dz}(SuA) = 0 \quad , \quad (39)$$

$$\frac{du}{dz} = \frac{\sum_{i=1}^j \sigma_i R_i - \frac{u}{A} \frac{dA}{dz}}{1 - u^2/c^2} \quad , \quad (39)$$

$$\frac{d\lambda_i}{dz} = R_i/u \quad , \quad (40)$$

$$\text{and} \quad \frac{d}{dz}(H + u^2/2) = 0 \quad . \quad (41)$$

Several authors have taken the above equations with realistic rate terms and applied computer methods to obtain a variety of results. Some of this work is summarized in Chapter 5 of Ref. 6. Wecken<sup>11</sup> takes

$$\frac{1}{A} \frac{dA}{dz} = \epsilon = \text{constant} \quad , \quad (42)$$

with one Arrhenius reaction to discuss the structure of the reaction zone. He is not successful in obtaining detonation failure at some critical  $\epsilon$  because of computational difficulties. Tsuge et al.<sup>12</sup> take

$$\frac{dA}{dz} = \frac{1}{\sigma_1} \left[ \frac{P_g - A}{(1 + 8kM_0^2)A - P_g} \right]^{1/2} \quad , \quad (43)$$

where  $\sigma_1$  is the value of the thickness  $\sigma$  of an explosive slab at  $Z = 0$ ,  $g$  is given in Eq. (16) ,

$$A = \frac{\sigma}{\sigma_1} \quad , \quad P = \frac{p}{p_1} A \quad , \quad \text{and} \quad k = \frac{p_{01}}{p_0} \quad , \quad (44)$$

where  $\rho_{\infty}$  is the density of the confining medium. Eq. (43) is obtained by treating the lateral expansion as a blunt body about which the confining inert flows. Tsuge et al. take a very detailed description of the reaction kinetics for  $H_2 + \frac{1}{2} O_2 \rightarrow H_2O$  and solve the problem numerically. Their com-

parisons with experiment for exploding slabs are fairly good. Their numerical calculations lead to plots as shown in Fig. 3. For  $\sigma_1 < \sigma_c$  there is no detonation solution, so detonation failure is found in this model. For  $\sigma_1 > \sigma_c$  they obtain two solution branches. The upper branch is like the usual 1-dimensional detonation  $M_{0+}$  of Eq. (36). They did not explore the lower branch fully because of computational difficulties. They speculate that as  $\sigma_1 \rightarrow \infty$  the lower branch has  $M_0 \rightarrow 1$ . It will be shown here that this is incorrect. The limit of the lower branch as  $\sigma_1 \rightarrow \infty$  is actually  $M_0 \rightarrow M_{0-}$  as in Eq. (36).

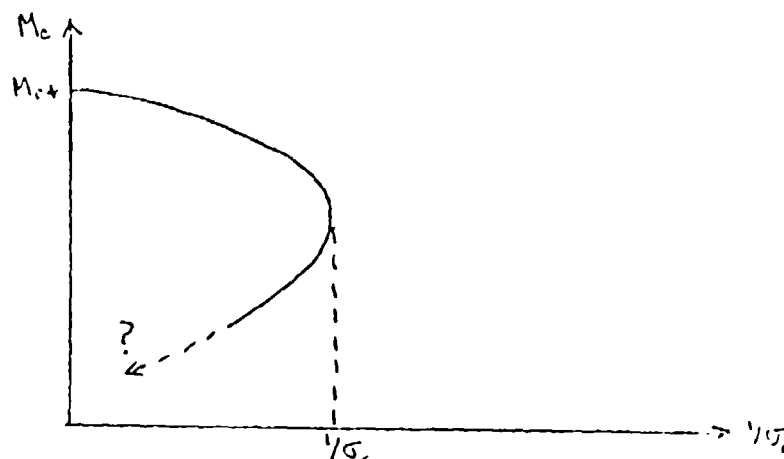


Fig. 3. Rough plot of  $M_0$  vs.  $1/\sigma$  in Tsuge et al.<sup>12</sup>

Rather than attacking this problem numerically from the beginning we will try to develop the solution analytically as far as possible. We use the equation of state given in Eq. (6). Then the  $\sigma_i$  defined in Eq. (26) (not to be confused with the  $\sigma$  and  $\sigma_1$  above which were lengths) are given by

$$\sigma_i = \frac{(\gamma-1)}{c^2} q_i, \quad (45)$$

where

$$c^2 = \frac{\gamma-1}{\gamma} = \frac{2(\gamma-1)}{2 + (\gamma-1)\gamma} \left[ \sum_i \lambda_i z_i + H + u^2/2 \right]. \quad (46)$$

We rewrite Eq. (39) as

$$\frac{2(1-m)}{m(1+\gamma m)[2+(\gamma-1)m]} \frac{dm}{dz} = \frac{\frac{d}{dz} \sum_i \lambda_i q_i}{\sum_i \lambda_i q_i + H_1 + u^2/2} - \frac{2}{1+\gamma m} \frac{1}{A} \frac{dA}{dz},$$

where  $m = M^2 = u^2/c^2$  (47)

Eq. (47) is to be solved so that  $dm/dz$  remains finite at  $m=1$ . A necessary

condition for this is that the right hand side of Eq. (47) be zero when  $m=1$ . Also at  $Z=0$ ,  $\lambda=0$  and  $m=m_1$  with  $m_1$  to be determined. These are unusual boundary conditions to impose on a first order ordinary differential equation. Eq. (47) does not satisfy the usual Lipschitz condition needed for the existence of a solution with a desired value of  $m$  at a specific  $Z$ . But the unusual boundary conditions are sufficiently "free" that a solution will exist. We do not fix the  $Z$  where  $m=1$  occurs, the sonic point  $Z$ , but we let the equation tell us so as to keep  $dm/dz$  finite. Then we find the value  $m_1$ . Since the problem presented by Eq. (47) is not a standard one it is unclear that a Picard iteration method will converge for it. We have found useful results with this method, so we will use it with the awareness that it may need modification due to convergence difficulties. The  $n^{\text{th}}$  iteration of  $m$ ,  $m^n$  will be found from

$$\frac{2(1-m^n)}{m^n(1+\gamma m^n)[2+(\gamma-1)m^n]} \frac{dm^n}{dz} = \frac{\frac{d}{dz} \sum_i \lambda_i^n q_i}{\sum_i \lambda_i^n q_i + H_1^n + u^n^2/2} - \frac{2}{1+\gamma m^{n-1}} \frac{1}{A} \frac{dA}{dz}, \quad (48)$$

where  $n = 2, 3, \dots$

with the right hand side of Eq. (48) equal to zero when  $m^n = 1$ . We also need to use Eq. (40). The first iterate  $m^1$  is found by putting the  $dA/dz$  term equal to zero. The equation for  $m^1$  can be integrated to get

$$\frac{m' [z + (\gamma - 1) m'] [1 + \gamma m']^2}{(1 + \gamma m')^2 m' [z + (\gamma - 1) m']} = \frac{\sum \lambda_i q_i + \frac{c_1^2}{2(\gamma - 1)} [z + (\gamma - 1) m']}{\frac{c_1^2}{2(\gamma - 1)} [z + (\gamma - 1) m']} , \quad (49)$$

where  $m'_1 = m'(z=0) , \quad (50)$

and where we have used Eq. (46) evaluated at  $Z=0$  , with  $c_1 = c(Z=0)$ .  
Imposing the right hand side condition for the  $m$  equation we get

$$\frac{d}{dz} \sum_{i=1}^j \lambda_i q_i = 0 \quad \text{at} \quad m' = 1 . \quad (51)$$

If all the  $q_i$  are positive, and the  $R_i$  are as given in Eq. (5), we need that for the first iteration, at the sonic point  $Z_s^1$  ,

$$m'(Z_s^1) = 1 , \quad \lambda_i(Z_s^1) = 1 . \quad (52)$$

For the simple  $R_i$  this implies  $Z_s^1 = \infty$  . We go to Eq. (49) and put  $\lambda_i = 1$  when  $m' = 1$  to find  $m'_1$  . The result is that  $m'_1$  obeys the equation

$$\frac{(1 + \gamma)(1 + \gamma m'_1)}{(1 + \gamma)^2 m'_1} = [z + (\gamma - 1) m'_1] + \frac{2(\gamma - 1)}{c_1^2} \sum_i q_i . \quad (53)$$

Manipulating this equation yields

$$(m'_1)^2 - 2 m'_1 \left[ 1 + \frac{(\gamma^2 - 1)}{c_1^2} \sum_i q_i \right] + 1 = 0 . \quad (54)$$

Eq. (54) is almost the same as Eq. (35). The difference is that in Eq. (35) we have  $c_0$  and  $D = M_0 c_0$  whereas  $c_1$  appears in Eq. (54). If we consider the case with no shock, then  $c_1 = c_0$ ,  $m_1^1 = m_0^1$ , and we have the same result as in Eq. (35). The solutions obtained would refer to a no-shock detonation that goes along O-CJ+ and a no-shock deflagration that goes along O-CJ-. The second of these is meaningful, but not the first. If we consider the case with a shock we put

$$c_1^2 = \frac{\gamma p_1}{\rho_1} = \frac{\gamma p_0}{\rho_0} \frac{[2\gamma m_0' - (\gamma-1)][2 + (\gamma-1)m_0']}{(\gamma+1)^2 m_0'} \quad (55)$$

into Eq. (54) to get, after using Eq. (15),

$$(m_0')^2 - 2m_0' \left[ 1 + \frac{\gamma^2 - 1}{C^2} \sum_i q_i \right] + 1 = 0 \quad (56)$$

This is exactly the same as Eq. (35), just as it should be because the R+ line in Fig. 2 is the same whether we consider a shock solution along O-N-CJ+, or a no shock one along O-CJ+. The two solutions of Eq. (56) are interpreted as a Von Neumann detonation along O-N-CJ+, and an unphysical shocked deflagration along O-S-CJ-. Out of the four solutions obtained we only desire the shocked detonation O-N-CJ+, and the no-shock deflagration O-CJ-. Their detonation velocities are given by the roots  $D_+ = c_0 M_{0+}$  and  $D_- = c_0 M_{0-}$  of Eq. (35). Using Eq. (15) we get the  $m_{1+}^1$  that goes with  $M_{0+}$  while the  $m_{1-}^1$  that goes with  $M_{0-}$  is  $m_{1-}^1 = M_{0-}$ . Knowing  $m_{1+}^1$  and  $m_{1-}^1$  we go to Eq. (49) and we get  $m_+^1$  and  $m_-^1$  as functions of  $\lambda_1(z)$ . Finally from Eq. (40) we can integrate to get  $\lambda^1(z)$ . This first iterate reproduces the results of Sec. IV because  $d\Lambda/dz$  was neglected. But we begin to see the source of the two roots in the work of Tsuge et al.<sup>12</sup> When we compute the next iteration the results of the expansion will come in. But as the diameter goes to  $\infty$  the expansion becomes negligible and the results reduce to  $m_+^1$  and  $m_-^1$ . To compute  $m^2$  we go to Eq. (40) with  $n=2$ . We integrate it with the boundary condition

$$m^2(z=0) = m_1^2 \quad (57)$$

The result is

$$\ln \left\{ \frac{m^2 [z + (\gamma-1)m^2] (1 + \gamma m^2)^2}{(1 + \gamma m^2)^2 m_1^2 [z + (\gamma-1)m_1^2]} \right\} = \ln \left\{ \frac{\sum_i \lambda_i^2 q_i + H_1^2 + (u_1^2)/2}{H_1^2 + (u_1^2)/2} \right\} - 2 \int_0^z \frac{1}{1 + \gamma m^2} \frac{1}{A} \frac{dA}{dz} dz \quad (58)$$

$m_1^2$  is determined by imposing the bounded  $dm^2/dz$  condition to the right hand side of Eq. (48) with  $n=2$ . At the sonic point  $z_s^2$  we have

$$\frac{1}{\sum_i \lambda_i^2 q_i + H_1^2 + (u_1^2)/2} \sum_i q_i \left( \frac{1 - \lambda_i^2}{c} \right) F_i \Big|_{z_s^2} = \frac{1}{1 + \gamma m_1^2} \frac{1}{A} \frac{dA}{dz} \Big|_{z_s^2} \quad (59)$$

Eq. (40) was used to obtain Eq. (59). The latter equation says that  $\lambda_i \neq 1$  at the sonic point so the reactions are not completed. Some of the energy will be released late leading to nonideal behavior. In principle Eq. (59) determines  $z_s^2$  in terms of  $m_1^2$ . This can be seen as follows. We have that

$$\left. \frac{(c)^2}{\gamma-1} + \frac{(u)^2}{2} \right|_{z_s^2} = H_1 + \frac{(u_1)^2}{2} = \left. \frac{(c)^2}{\gamma-1} + \frac{(c)^2}{2} \right|_{z_s^2}, \quad (60)$$

so that  $c$  in Eq. (59) is known in terms of  $m_1^2$  and  $c_1$ . Also from Eq. (40)

$$\frac{d\lambda_i^2}{dz} = \frac{R_i}{m^2 c} \quad (61)$$



In Eq. (61)  $m^2$  is known in terms of  $\lambda^2$  from Eq. (58). (We assume that  $\frac{1}{A} \frac{dA}{dz}$  is explicitly known as a function of  $Z$ ). Therefore one can integrate Eq. (61) to get  $\lambda^2$  as a function of  $Z$  and  $m_1^2$ . When this function  $\lambda^2(Z, m_1^2)$  is substituted into Eq. (59) one can find  $Z_S^2$  as a function of  $m_1^2$  as claimed. Now we go back to Eq. (58) and demand that

$$m^2(z_s) = 1, \quad \lambda_s^2(z_s) = \lambda_i^2(z, m_1^2) \equiv \lambda_i, \quad (62)$$

and get

$$\frac{(1 + \gamma m_1^2)^2}{(1 + \gamma) m_1^4} = 2 + (\gamma - 1) m_1^2 + \frac{2(\gamma - 1)}{(c_i)^2} \sum \lambda_{is} q_i - 2[z + (\gamma - 1) m_1^2] \int_0^{z_s^2} \frac{1}{1 + \gamma m_1^2} \frac{1}{A} \frac{dA}{dz} dz. \quad (63)$$

In Eq. (63)  $Z_S^2$  and  $\lambda_s^2$  are functions of  $m_1^2$ . So Eq. (63) is an equation for  $m_1^2$ . The last term is the expansion dependent term. Let

$$\Delta(\epsilon) = 2 \int_0^{z_s^2} \frac{1}{1 + \gamma m_1^2} \frac{1}{A} \frac{dA}{dz} dz. \quad (64)$$

Here  $\epsilon$  represents an inverse diameter that goes to zero as the diameter goes to  $\infty$ . Also  $\Delta(\epsilon) \rightarrow 0$  as  $\epsilon \rightarrow 0$  or as the expansion is negligible. Eq. (63) is rewritten as

$$(m_1^2)^4 [1 + (\gamma^2 - 1) \Delta] - 2 m_1^2 \left[ 1 + \frac{\gamma^2 - 1}{(c_i)^2} \sum \lambda_{is} q_i - \Delta(1 + \gamma) \right] + 1 = 0. \quad (65)$$

This equation reduces to Eq. (54) as  $\Delta \rightarrow 0$  and  $\lambda_s^2 \rightarrow 1$  as  $\epsilon \rightarrow 0$ . Thus there is a clear connection between the two branches to be obtained from Eq. (65) and the 1-dimensional results. The two roots of Eq. (65) are obtained by the quadratic formula as

$$m_1^2 = \frac{\left[ 1 + \frac{(\gamma^2 - 1)}{(c_i)^2} \sum \lambda_{is} q_i - \Delta(1 + \gamma) \right] \pm \sqrt{\left[ 1 + \frac{(\gamma^2 - 1)}{(c_i)^2} \sum \lambda_{is} q_i - \Delta(1 + \gamma) \right]^2 - [1 + \Delta(\gamma^2 - 1)]}}{[1 + \Delta(\gamma^2 - 1)]}. \quad (66)$$

For small  $\epsilon$  these two roots give the  $m_+^1$  and  $m_-^1$  of before which were connected with the  $m_{0+}^1$  and  $m_{0-}^1$  of Eq.(35). As  $\epsilon$  and  $\Delta$  grow beyond a critical value the two roots become complex, so there is no real solution and detonation failure takes place. To simplify things let us ignore the variation of  $\lambda_S^2$  with  $\epsilon$ . Then a plot of the roots versus  $\Delta$  appears as in Fig. 4. This is qualitatively the same as the curve  $\Delta M$

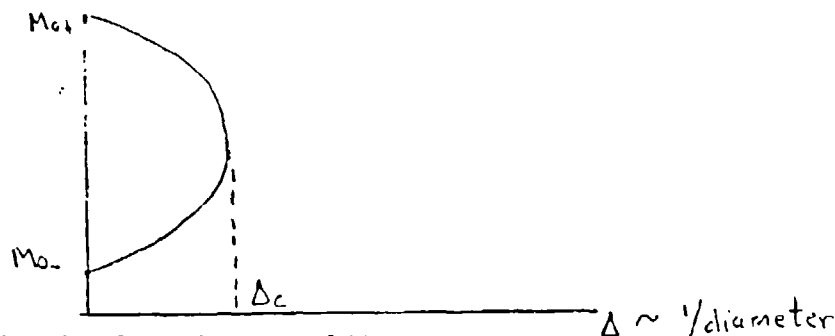


Fig. 4. Plot of  $M_0$  vs.  $1/\text{diameter}$ .

obtained numerically by Tsuge et al. For  $\Delta < \Delta_c$  (for the diameter greater than some critical value) there are two branches. The upper branch is connected as  $\Delta \rightarrow 0$  to the 1-dimensional shocked detonation O-N-CJ<sub>+</sub> of Fig. 2. The lower branch is connected as  $\Delta \rightarrow 0$  to the 1-dimensional no-shock deflagration O-CJ<sub>-</sub>. Now one sees the error in the work Tsuge et al. They could compute things like  $Z_S^2$  and  $\lambda_S^2$  numerically but with so much difficulty that the results were hard to interpret.

The qualitative features of the solution are now clear. To get quantitative results one needs to integrate Eq. (61). This would have to be done numerically. It is clear that successive steps in the iteration are not very different from the steps to calculate  $m^2$ . No theoretical problems with convergence should arise although this should be checked numerically in some specific examples. We propose to do this in future work. The critical value  $\Delta$  at which detonation failure occurs is given by

$$1 + (\gamma^2 - 1) \Delta_c \geq \left[ 1 + \frac{\gamma^2 - 1}{(\gamma^2 - 1)} \sum \lambda_i^2 q_i - (1 + \gamma) \Delta \right]^2. \quad (67)$$

It would be interesting to explore ways in which this behavior could be checked with experiment. It should be noted that this theory predicts that the speed of deflagrations increases as the diameter decreases. At some critical diameter the detonation and deflagration velocities are the same and for smaller diameters there is no solution.

## VI CONCLUSIONS AND RECOMMENDATIONS

The causes of nonideal behavior can be summarized in three categories.

- (i) Incompletely effective use of the chemical energy for the detonation wave due to the nature of the chemical reactions. If there are reversible or endothermic reactions, the effects are especially important. For steady 1-dimensional flows the physical theory is prepared to handle the problem. The knowledge of the burning rates of the relevant chemical reactions, however, needs to be improved.
- (ii) Loss of strength due to the lateral expansion of the explosive. Here the state of the physical theory is not so good. In Sec. V we presented a calculation for detonation failure. The radial flow was not calculated but was assumed known. The analytical solution presented should be checked with numerical calculations. A further step would be to compare these results with experiment. The author would like to be able to pursue these further developments.
- (iii) Loss of strength due to transverse structure of the front and non-steady phenomena in the detonation. These effects are interesting per se and their effects on nonideal behavior are judged to be important<sup>6</sup>. These wave instability problems were not addressed in this research effort because the author felt he needed a good understanding of the simpler aspects of nonideal behavior before addressing them. There is much room for research into these effects using the techniques of nonlinear stability analysis and bifurcation theory.